

Swarmodroid 1.0: A Modular Bristle-Bot Platform for Robotic Active Matter Studies

Alexey A. Dmitriev,^{1,*} Alina D. Rozenblit,^{1,*} Vadim A. Porvatov,^{2,3,*} Mikhail K. Buzakov,¹
Anastasia A. Molodtsova,¹ Daria V. Sennikova,¹ Vyacheslav A. Smirnov,¹
Oleg I. Burmistrov,¹ Timur I. Karimov,⁴ Ekaterina M. Puhtina,¹ and Nikita A. Olekhno^{1,†}

¹*School of Physics and Engineering, ITMO University, Saint Petersburg 197101, Russia*

²*Department of Infocommunication Technologies,*

National University of Science and Technology "MISIS", Moscow 119991, Russia

³*Faculty of Science, University of Amsterdam, Amsterdam 1098 XH, Netherland*

⁴*Department of Computer-Aided Design, Saint Petersburg Electrotechnical University "LETI", Saint Petersburg 197376, Russia*

(Dated: May 24, 2023)

Large swarms of extremely simple robots (i.e., capable just of basic motion activities, like propelling forward or self-rotating) are widely applied to study collective task performance based on self-organization or local algorithms instead of sophisticated programming and global swarm coordination. Moreover, they represent a versatile yet affordable platform for experimental studies in physics, particularly in active matter – non-equilibrium assemblies of particles converting their energy to a directed motion. However, a large set of robotics platforms is being used in different studies, while the universal design is still lacking. Despite such platforms possess advantages in certain application scenarios, their large number sufficiently limits further development of results in the field, as advancing some study requires to buy or manually produce the corresponding robots. To address this issue, we develop an open-source Swarmodroid 1.0 platform based on bristle-bots with reconfigurable 3D-printed bodies, external control of motion velocity, and basic capabilities of velocity profile programming. In addition, we introduce AMPy software package in Python featuring OpenCV-based extraction of robotic swarm kinematics accompanied by the evaluation of key physical quantities describing the collective dynamics. We perform a detailed analysis of individual Swarmodroids' motion characteristics and address their use cases with two examples: a cargo transport performed by self-rotating robots and a velocity-dependent jam formation in a bottleneck by self-propelling robots. Finally, we provide a comparison of existing centimeter-scale robotic platforms, a review of key quantities describing collective dynamics of many-particle systems, and a comprehensive outlook considering potential applications as well as further directions for fundamental studies and Swarmodroid 1.0 platform development.

I. INTRODUCTION

Modern progress in physics unveils the novel area in swarm robotics that focuses on engineering an emergent collective behaviour instead of the programming of individual robots. One set of examples includes applied tasks. At the macroscale, collective functions such as cargo transport by large swarms of robots can be implemented with the help of statistical control [1], placing self-propelled robots in flexible boundaries [2, 3], an engineered rattling [4, 5], and cohesive interactions [6]. Further miniaturization allows realizing experiment automation at millimeter scales [7], microplastics removal [8, 9], and even medical applications of particle swarms [8] at the microscale. On the other hand, there are numerous studies of statistical many-particle physics, especially in the area of active matter, that rely on large swarms of BEAM robots (from biology, electronics, aesthetics, and mechanics). Such studies consider phase transitions [10], topological edge states [11], or even emulate the dynamics of financial markets [12]. Somewhere in-between of the

areas of swarm robotics and physics lie various works that address machine learning-based control of such swarms of simple robots [13] or experimentally implement local algorithms rather resembling cellular automation [14].

However, most of these works utilize an excessive number of robotic platforms with different design and capabilities. For example, the papers which are closer to cybernetics and consider collective swarm functions usually rely on custom author-developed hardware, like Refs. [1, 6]. In turn, a common practice in experiments on many-particle physics is to use rather simplistic toy robots HEXBUGs® [2, 10, 11, 15], rarely introducing custom bristle-bots [16]. Finally, many works employ Kilobots [17] that are comprehensive, affordable, and mass-produced, yet cannot move fast enough for certain use cases and lack reconfigurability.

Despite the domain-specific advantages of each robotic platform, their large number restricts further development of results because of the need to use specific robots for each study. Moreover, it complicates the verification of data from papers in the field which is a cornerstone of the scientific approach. Finally, in many cases certain robots possess redundant functionalities not required in the considered application scenarios, thus considerably increasing the cost of experiments. The raised points result in a considerable demand for an open *golden mean* platform preserving an optimal trade-off between sim-

* Alexey A. Dmitriev, Alina D. Rozenblit, and Vadim A. Porvatov contributed equally to this work

† nikita.olekhno@metalab.ifmo.ru

plicity and versatility.

In this Paper, we introduce a swarm robotics platform which we call Swarmodroid 1.0. The developed platform features USB-rechargeable bristle-bots with remotely controlled motion velocity, reconfigurable plastic bodies and motion patterns, and a comprehensive Python processing software in AMPy package to study swarm kinematics, all distributed under GPL v3 license [18]. The developed platform relies on a single-layer printed circuit board production, additive manufacturing, and the use of widely spread and affordable components. Thus, we hope that it may find broad use in performing experiments with robotic swarms featuring a large number of robots.

The Paper is organized as follows. In Section II, we describe the overall structure of the experimental setup as well as basic building blocks of an individual Swarmodroid. Then, in Section III, we focus on the Swarmodroid printed circuit board design and its programming. Section IV introduces the processing software within AMPy package and provides a detailed overview of the quantities describing collective properties which are evaluated by our software. Section V addresses the kinematic characteristics of individual Swarmodroids in different regimes and their statistical averaging over several robots. In Section VI, we compare the existing alternatives to the presented platform. Next, in Section VII, we consider two potential use cases of the proposed platform for implementing a collective cargo transport and studying a velocity-mediated jamming of robots in a bottleneck. Finally, potential applications and directions of future development are summarized in Section VII.

II. ROBOT DESIGN

Experimental setup for studying collective effects in robotic swarms typically includes a barrier enclosing some area in which robots move and a set of robots, Figure 1(a). In our case, the setup is supplied with Sony ZV-E10 HD camera capturing the motion of robots. Then, the locations of ArUco markers placed at the center of top surface of each robot are extracted with the help of OpenCV library and processed by the introduced AMPy software package, Figure 1(c).

The Swarmodroid body consists of several plastic elements including a cap with ArUco marker, a base to which the printed circuit board (PCB) is attached, and bristles which convert the vibration of robot's motor to a directed motion ¹, see Figure 1(a). All these parts are produced via fused deposition modeling (FDM) technology using Flying Bear Ghost 5 3D-printers with nozzle diameter 0.4 mm. As the printing material, PLA plastic with a melting point around 200°C was chosen. Further,

we address in detail two particular variations of Swarmodroids.

Circular-shaped self-rotating robots (Type-I) For such robots, the base has a form of a circular plate with the diameter of 46 mm and the thickness of 1.5 mm, Figure 1(e). The base features a section for a rechargeable battery in the centre, round holes for screws attaching the circuit board and the cap, and several rectangular holes matching the elements of PCB such as a USB-port for charging. The top surface of the base is totally flat, while the bottom one contains protrusions for the attachment of bristles and a battery. The bristles can be attached in two configurations allowing to implement the self-propelled and self-rotating types of motion, respectively. In the first case shown in the inset of Figure 1(a), two lines of bristles inclined by 10° with respect to the surface normal are attached to straight grooves, while in the second case, the bristles with the same inclination angle are attached in one closed line along the edge of the base, as in Figure 1(e). In such a case, clockwise or counter-clockwise rotation of the robots is defined by the slope direction. For both configurations, a single bristle has the dimensions of 7.5 × 0.8 × 0.4 mm.

The cap has a cylindrical shape with the diameter $d = 48.7$ mm, the height of 19.2 mm, and the wall thickness of 0.6 mm. The top surface of the cap features technological holes providing access to the switcher allowing to manually turn the robot on and off and LEDs indicating the state of the robot. Also, there are two pillars inside the cap containing a section for a nut and a hole for a screw, and one additional supporting pillar attached to the base via the corresponding notch. The height of the pillars is 10.1 mm, which corresponds to the height of cap's top surface with respect to the base. The rest height of the cap's side surface partially covers the bristles in order to increase the stability of the robot. The aperture on the side surface of the cap allows charging robots without disassembling them.

In bristle-bot design, flexible bristles play a crucial role by converting the vibration of a motor to the motion of a robot. Despite in our case the bristles are made of a rigid PLA plastic to simplify the robot's production by using the same material for all parts, they are still flexible enough due to their small thickness of 0.4 mm. As shown in Ref. [19], such PLA bristles even outperform bristles made of BFlex resin-like material when implementing self-rotating robots. A bristle inclination angle of 10° is also chosen as an optimal value for PLA bristles based on the above reference, also taking into account the results of work [16].

Stadium-shaped self-propelled robots (Type-II) The base in such robots has a racetrack-like geometry with axes 82.6 mm and 45 mm, respectively. The location of PCB is shifted from the geometrical center, yet the circuit board is attached in the same manner as for Type-I Swarmodroids. However, larger size of the base and cap compared to self-rotating design allows to implement the assembly of these two parts via neodymium magnets in-

¹ <https://github.com/swarmtronics/swarmodroid.pcb>

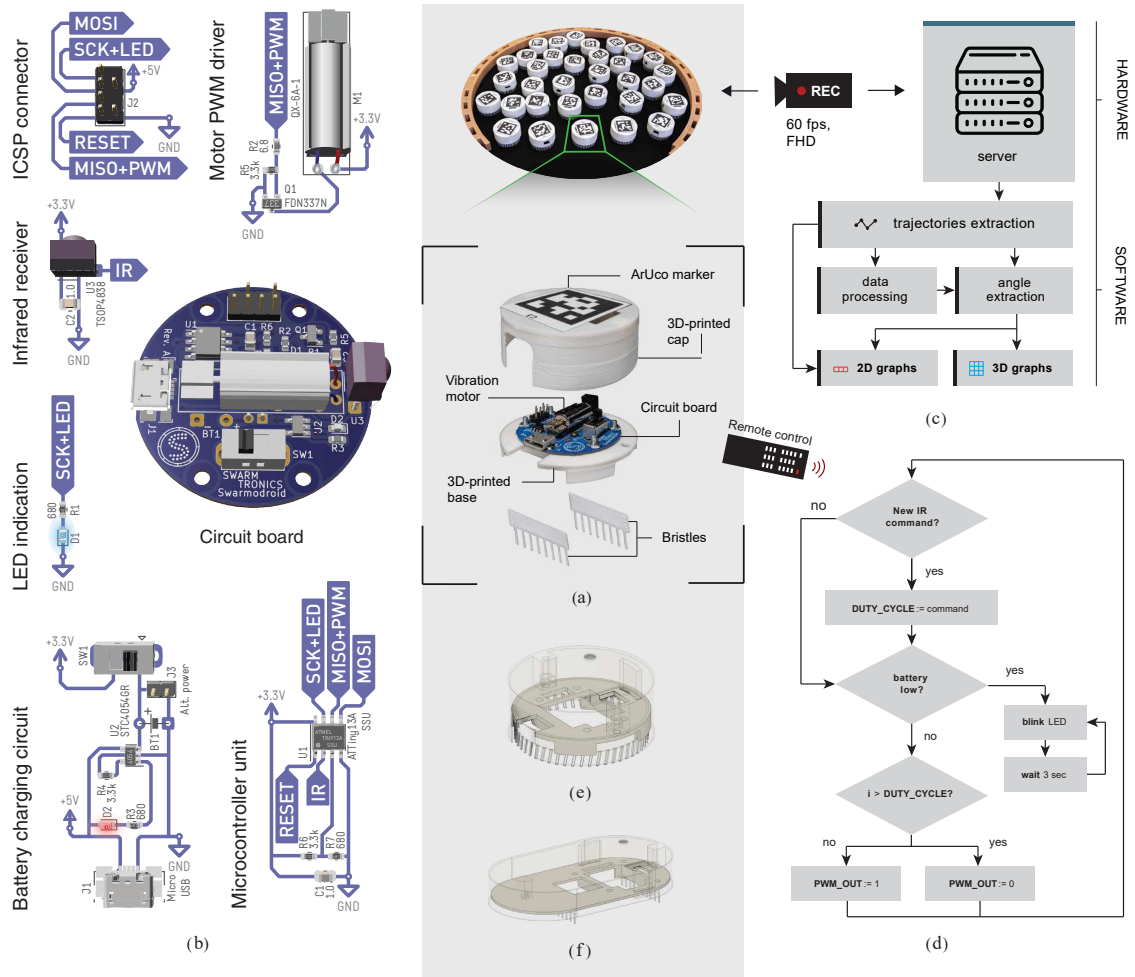


Figure 1. Schematics of the Swarmdroid platform. (a) Robotic swarm confined in a circular-shaped barrier (top) and the burst diagram of a single robot (bottom). The robot consists of a 3D-printed cap, base, bristles, and a printed circuit board with a vibration motor. Individual ArUco markers are placed on the top surfaces of robots. (b) Diagram of the control circuit along with its render (in the center). (c) Processing software diagram. The motion of robots is captured with the help of an HD camera, and the locations of ArUco markers are extracted via OpenCV library. Then, various quantities characterizing single-robot dynamics as well as collective behavior are evaluated. (d) Diagram of the Swarmdroid boot executed at ATTiny13 microcontroller at the circuit board. The robot checks the presence of a command from IR remote controller, and, if present, adjusts its motion velocity. Besides, the battery level is checked and displayed via the LEDs. (e,f) Different designs of 3D-printed bodies corresponding to cylindrical self-rotating Type-I Swarmdroids (e), similar to those in Panel (a), and to elongated self-propelled Type-II Swarmdroids (f). Both types are assembled with the same circuit board from Panel (b).

instead of screws. We apply the magnets having a cylindrical shape with the diameter of 3 mm and height of 2 mm. The magnets locate at the opposite edges of the robot on its larger axis and are placed in the slots of a corresponding geometry in the base and cap. The bottom side of the base has three straight grooves in which the bristles are placed, with grooves being inclined at the angle of 10° with respect to the surface normal. However, to achieve an efficient self-propelled motion, it is sufficient to use just two sets of bristles placed at the outermost grooves.

In the following, we study the properties of Type-I and Type-II Swarmdroids and perform two sets of experiments with large robotic collectives, one with self-

rotating Type-I robots and the other one with self-propelling Type-II. However, there are unlimited possibilities to design various shapes of robots while using the same circuit board and maintaining the compatibility with recognition software.

III. ROBOT CIRCUITRY

The circuit diagram is shown in Fig. 1(b). It can be divided into the following structural blocks: (i) battery and the charging circuit, (ii) LED indication, (iii) motor pulse-width modulation (PWM) driver, (iv) infrared

receiver, (v) microcontroller unit (MCU), and (vi) in-circuit serial programming (ICSP) connector, all located at (vii) the printed circuit board (PCB).

(i) *Battery and charging circuit* All electric components are powered by Robiton LP601120 100 mAh lithium-ion polymer battery (BT1); hereafter, labels in brackets denote the corresponding parts in Fig. 1(b). The SS12D07 hard poweroff switch (SW1) shuts down the robot by disconnecting the battery from the circuit. Battery charging can be performed from any 5 VDC source that can supply a 300 mA current, through a Micro USB connector (J1), or, alternatively, through the ICSP connector (J2). The actual charging current and voltage delivered to the battery cell are controlled by the charge control circuit STMicroelectronics STC4054GR (U2), which limits the charging current to 300 mA during the constant-current charging phase and the charging voltage to 4.2 V during the constant-voltage charging phase. Additionally, a footprint for a PLS2-2 pin header (J3) is provided for connecting alternative power sources (such as laboratory power sources, wireless charging coils, etc.), but the pin header itself is not installed if the battery is used.

(ii) *LED indication* The LED indication consists of two 0603 surface-mount LEDs (D1) and (D2) with current-limiting resistors (R1) and (R2). The LED (D1) serves as a general-purpose indication and is switched by the MCU. It displays the following signals: (a) shining constantly – robot is running; (b) turned off robot switched off; (c) briefly turned off – receiving a command from IR remote control; (d) blinking one, two or three times – battery level 30%, 60% or 100% respectively; (e) blinking briefly once every three seconds – battery level below critical, need to charge the robot immediately to avoid battery overdischarge. The LED (D2) is driven by the charge controller (U2) and only has two states: (a) shining – battery is now charged, (b) turned off – charge finished (charging current fell below 30 mA) or charger not connected.

(iii) *Motor PWM driver* The robot is actuated by the vibration motor QX Motor QX-6A-1 (M1). Different motion velocities are implemented by limiting the average motor power to the selected percentage by Onsemi FDN337N n-MOSFET switch (Q1) that is driven with a pulse-width modulated signal. The gate of transistor (Q1) is pulled down to the source by the resistor (R5) to prevent spontaneous opening. The resistor (R2) acts as a gate current limiter. The PWM signal has the frequency of approximately 70 Hz and 3.3 V CMOS logic level. The PWM duty cycle allows 256 steps, from 0% (completely off) to 100% (completely on). In the limiting cases of 0% and 100% duty cycles, the PWM switching is turned off, and a constant gate voltage is provided instead.

(iv) *Infrared receiver* To capture commands sent by an infrared remote control device, Vishay TSOP4838 infrared receiver (U3) is used. The circuit is designed to accept commands transferred by NEC infrared protocol [20]. The receiver (U3) receives a sequence of 38 kHz

pulse bursts of the infrared signal and sends a 3.3 V logic level signal to the MCU according to the following rule: logic low if a pulse burst is being received, logic high otherwise. The resulting logic pulse sequence is a portion of pulse-period modulated data, which is software-decoded by the MCU. A 1 μ F filtering capacitor (C2) is installed near the receiver (U3) to isolate the receiver from switching noise.

(v) *Microcontroller unit* The entire Swarmodroid circuit, excluding the charging subsystem, is controlled by the Microchip ATtiny13A-SSU AVR microcontroller (U1). It performs the following functions: generating the PWM signal that drives the (Q1) gate, accepting and decoding the signals from the IR receiver (U3), general-purpose indication via the LED (D1), and battery voltage supervision by measuring the voltage on the resistor divider (R6)-(R7) to prevent overdischarge. A 1 μ F filtering capacitor (C1) is installed near the MCU to reduce its sensitivity to switching noise.

The MCU firmware² performs the following actions. First, as soon as the robot is turned on, a self-test is performed to make sure that the battery voltage is above the critical level (approximately 3.3 V). If it is below this threshold, the robot enters the power-saving mode. Otherwise, the measured battery idle voltage is indicated by blinking the LED (D1) one time for a low charge level, two times for a medium level, and three times for a full charge, respectively. Then, the motor is tested by turning it on for a time period of 50 ms, and the LED is lit up constantly to indicate that the robot is ready. At this stage, the main code enters an infinite waiting loop (the main loop), which is broken out of when the battery voltage drops below the critical level. Upon such an event, the robot enters the power-saving mode.

While the main loop is running, the 8-bit timer/counter of the MCU (clocked at 18.75 kHz) is used simultaneously to generate the PWM signal, measure the pulse widths to demodulate the signal from the IR receiver, and to trigger periodic battery voltage checks. For a timing diagram, see Supplementary Materials [21]. In the main loop itself, no other action is performed but waiting for an interrupt event, which is caused by an incoming command accepted by the IR receiver (U3). The commands are received as a pulse-period modulated 32-bit sequences as defined by the NEC protocol (the 16-bit address variant is used in our case). Each logical level change on the (U3) output generates an interrupt event [22]. The demodulation is performed at the corresponding interrupt service routine of the MCU by measuring the time intervals between the falling pulse edges, using the 8-bit timer/counter. If the received command is valid according to the NEC protocol and its address part is equal to the hard-coded address constant of the robot, the corresponding action

² <https://github.com/swarmtronics/swarmodroid.firmware>

is taken. The basic use-case is pairing the robot with a TV remote control and using the digit keys to control the robot – in this case, the actions are to set the PWM duty cycle to $\text{Duty Cycle} = \text{Digit} \cdot 10\%$. The power button is used to set the duty cycle to zero, and the 0 button – to 100%. During the incoming IR pulse sequence, the LED (D1) is turned off to indicate a currently received command.

Finally, as soon as the battery voltage falls below the critical level, the robot is forced into the power-saving mode. In this mode, all interrupts are disabled, i.e., the robot becomes unresponsive to any commands; the motor is turned off by sending a constant logic low to the gate (Q1). Besides, the LED (D1) is turned off and blinked briefly every three seconds to indicate that the robot needs to be charged.

The flowchart as well as the complete description of the robot firmware is provided in the Supplementary Materials [21].

(vi) *ICSP Connector* The MCU can be reprogrammed by the serial peripheral interface (SPI) through an ICSP connector (J2) (the power switch (SW1) must be turned on during programming). Note that two of the (U1) pins share multiple functions: pin 6 drives the gate (Q1) and doubles as the SPI MISO pin, while pin 7 is used for indication by the LED (D1) and doubles as the SPI SCK pin. This approach allows to easily verify that a robot is actually being programmed: in a valid programming procedure, the motor vibrates and the LED rapidly blinks.

(vii) *Printed circuit board* All electric components are mounted on a printed circuit board (PCB) in the shape of a disk with the diameter 35 mm, made on a 0.8 mm-thick FR4 dielectric substrate with two-sided 18 μm copper layers. The PCB is mounted bottom side to the base top using four DIN-7985/ISO-7045 M2 \times 6 screws and DIN-439/ISO-4035 M2 nuts. For these screws, four mounting holes of 2.2 mm diameter are provided in the PCB. In turn, all electronic components aside from the battery are mounted on the top side of the PCB. The only component on the bottom side is the battery, which is fitted into a specially designed notch in the base and connects to the PCB using wires.

IV. AMPY EXPERIMENT PROCESSING SOFTWARE

Along with the hardware part of the platform, we introduce AMPy package for the video data processing³. The code is written in Python and evaluates various physical quantities underpinning the collective properties of the swarm, Figure 2.

First, the package allows to extract the coordinates and orientations of individual robots by recognizing ArUco

markers placed on top of each robot, Figure 1(b). As the evaluation of statistical characteristics relies on the coordinates of the centre of area filled with robots, we implemented a special widget allowing to obtain such a point by detecting four auxiliary markers placed at the barrier. In order to eliminate the video distortions influencing the visibility of ArUco markers, we linearly interpolate missing points during the preprocessing stage. After such an extension of initial trajectories, we determine the robots' orientations with the help of known positions of ArUco markers, Figure 3(a). The final part of the pipeline allows to extract different types of motion characteristics of robotic swarms, including displacement-based, correlations, and collision graph statistics, as outlined further.

A. Collision graph statistics

Average clustering coefficient [23] is the parameter measuring the density of the force chains induced by robots collision:

$$\bar{C} = \frac{1}{N} \sum_{i=1}^N C_i, \quad (1)$$

where C_i is the local clustering coefficient of i 'th node evaluated as follows:

$$C_i = \frac{1}{k_i(k_i - 1)} \sum_{j,k} A_{ij} A_{jk} A_{ki}, \quad (2)$$

where $k_i = \sum_j A_{ij}$, and \hat{A} denotes the adjacency matrix of the collision graph. As seen in Figure 3(b), higher values of \bar{C} correspond to larger number of contacts between touching robots within a cluster, i.e., to more rigid and densely packed clusters.

B. Displacement-based statistics

Average displacement [24] allows characterizing the motion type of robots, as demonstrated in Figure 3(c), and in Cartesian coordinates reads

$$x(t) = \frac{1}{N} \sum_{i=1}^N \sqrt{\left(x_0^{(i)} - x_1^{(i)}(t)\right)^2 + \left(y_0^{(i)} - y_1^{(i)}(t)\right)^2}, \quad (3)$$

where $(x_0^{(i)}, y_0^{(i)})$ is the initial position of the robot corresponding to the i 'th trajectory and $(x_1^{(i)}(t), y_1^{(i)}(t))$ is the position of the same robot at the moment t . For sparse systems characterized by ballistic motion, the robots move freely between rare collisions, and $x(t)$ features linear time dependence, see the first region in Figure 3(c). At larger densities, the robots frequently collide and change their motion direction, which results in diffusive dynamics characteristic of liquids [intermediate region in Figure 3(c)]. In this case, $x(t)$ demonstrates

³ <https://github.com/swarmtronics/ampy>

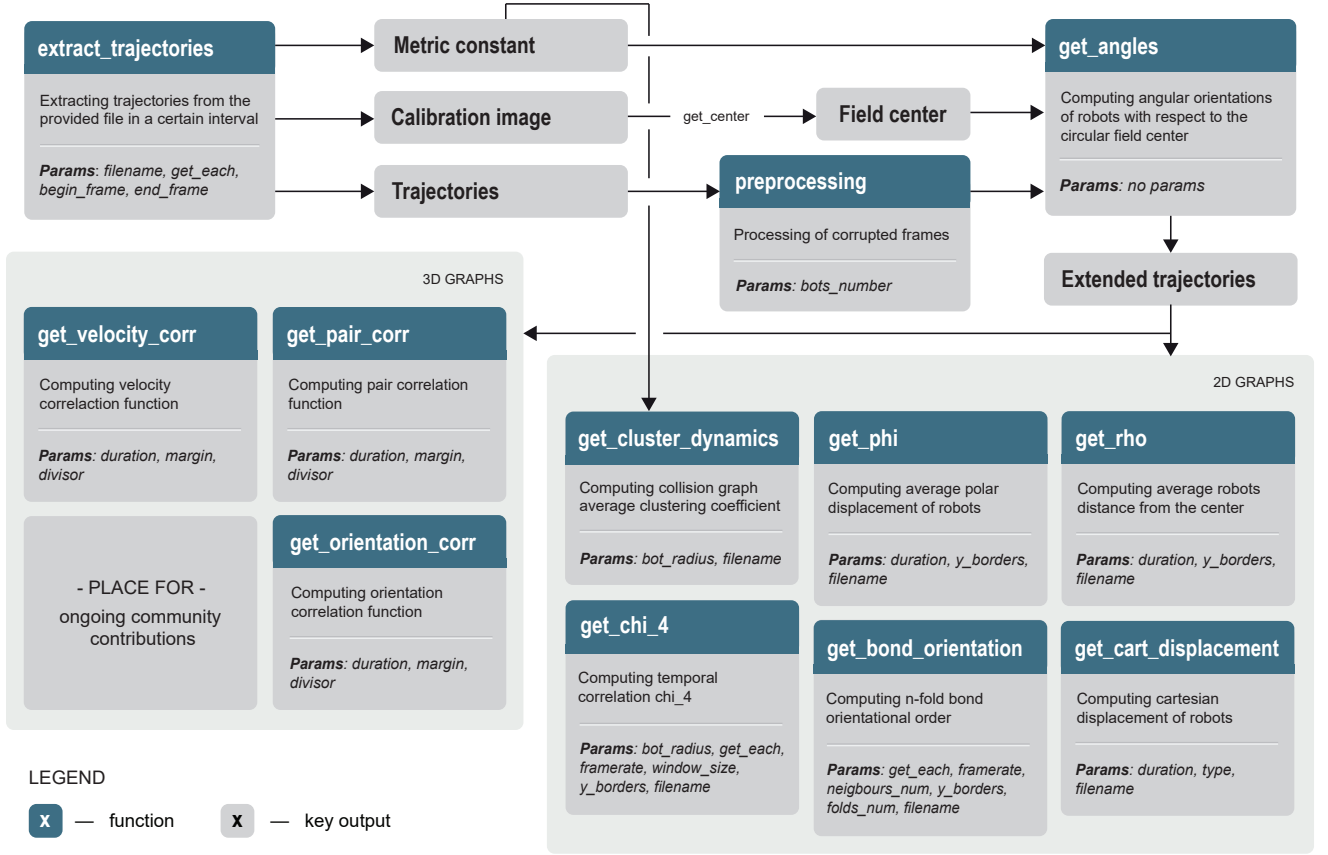


Figure 2. Software diagram illustrating the processing pipeline of experimental data. Each code block includes the name of the corresponding function, a brief description of its content, and a list of input parameters.

square root dependence on t . Finally, at very high densities, the robots form a rigid cluster and slightly fluctuate near their typical locations, with $x(t) \approx \text{const}$, as shown in the rightmost region in Figure 3(c).

For polar coordinates, we introduce the ρ parameter describing the average distance of robots from their initial positions with respect to the area center:

$$\rho(t) = \frac{1}{N} \sum_{i=1}^N \left(\rho_0^{(i)} - \rho_1^{(i)}(t) \right), \quad (4)$$

where $\rho_0^{(i)}$ is the distance between the centre of an area and the given robot at the moment $t = 0$ while $\rho_1^{(i)}(t)$ is the distance at the moment t . The parameter ϕ captures the dynamics of polar angle displacement:

$$\varphi(t) = \frac{1}{N} \sum_{i=1}^N \left(\phi_0^{(i)} - \phi_1^{(i)}(t) \right), \quad (5)$$

where $\phi_0^{(i)}$ is the initial polar angle of the given robot at the moment $t = 0$ and $\phi_1^{(i)}(t)$ is the polar angle at the moment t . For example, if ρ is constant while ϕ considerably changes, it highlights that the swarm rotates as a whole while slightly changing its geometry.

C. 2D correlation statistics

Sixfold index ψ_6 [25, 26] represents spatial ordering, i.e., time-independent spatial correlations:

$$\psi_6 = \left\langle \frac{1}{N_j} \sum_{j'} e^{i6\theta_{jj'}} \right\rangle_{\text{bulk}}, \quad (6)$$

where N_j is the number of robots touching j 'th robot and $\theta_{jj'}$ is the angle between vectors of j 'th and j' 'th robots. Operator $\langle \cdot \rangle_{\text{bulk}}$ denotes averaging over all robots, excluding those placed near the border. Such a quantity reaches high values if the structure of robots' packing resembles hexagonal crystal (e.g., a close packing of cylindrical Type-I Swarmodroids), Figure 3(d).

Spatio-temporal correlation parameter τ_* [26, 27] reflects the time-correlated spatial dynamics of the robots. It is defined by the four-point susceptibility order parameter χ_4 depending on the dynamical overlap function:

$$Q(t, \tau; a) = \frac{1}{N} \sum_{j=1}^N \Theta(a - |\hat{r}_j(t + \tau) - \hat{r}_j(t)|), \quad (7)$$

where a is the characteristic length chosen as the robot's

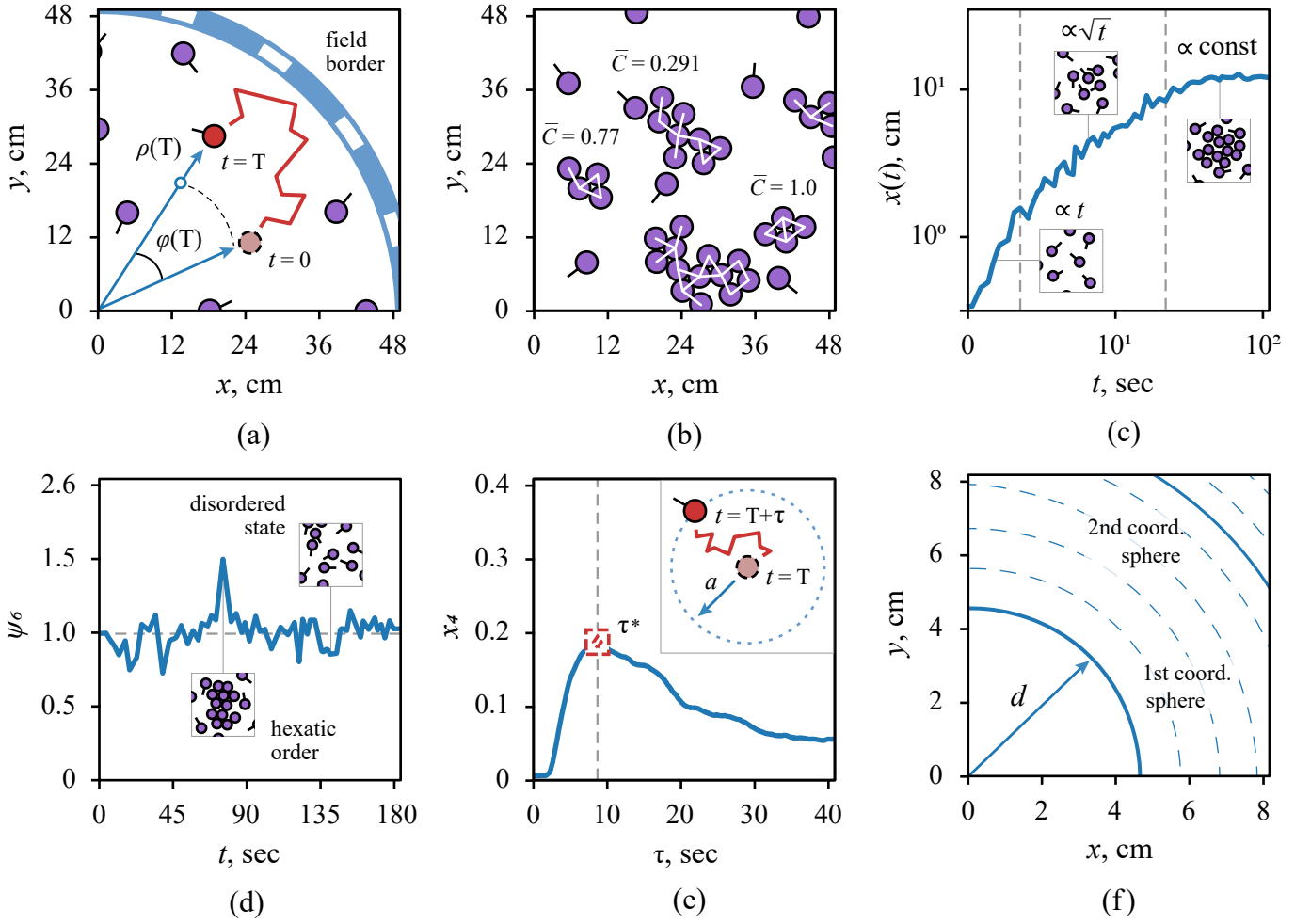


Figure 3. Illustration of different quantities extracted by the software. (a) Several robots (purple circles) placed in a circular barrier. The trajectory of a selected robot between timestamps $t = 0$ and $t = T$ is shown with red solid line, line segments near the circles denote velocity direction for each robot, $\rho(t)$ and $\varphi(t)$ are radius and polar angle of the robot in polar coordinates centered at the center of the barrier, respectively. (b) Several clusters of touching robots. Force chains are shown with white solid lines. The values of average clustering coefficient \bar{C} shown near the corresponding clusters are evaluated with Eq. (1). (c) Root mean square displacement $x(t)$ Eq. (3) schematically demonstrating the transition between ballistic (a linear region $x \propto t$), diffusive (a square root dependency $x \propto t^{1/2}$), and jamming (a saturated region $x \propto \text{const}$) behaviors. The insets show robotic swarm patterns with various densities characteristic of the corresponding motion types. (d) Sixfold index ψ_6 Eq. (6) demonstrating the transition between a disordered phase (low values) and hexatic order (peak). The insets demonstrate characteristic geometries of the system with and without a hexatic order. (e) Spatio-temporal correlation parameter τ^* Eq. (10) for a robot with the characteristic localization time close to 10 s. The inset demonstrates robot's trajectory between timestamps $t = T$ and $t = T + \tau$. (f) Sketch of the two-dimensional pair correlation function Eq. (11) for Type-I Swarmodroids showing characteristic circles at the distances of the robot diameter $d = 46$ mm (the first coordination sphere) and two robot diameters (the second coordination sphere) along with intermediate circles corresponding to other characteristic configurations of robots.

radius, t is the start timestamp, τ is the time from the start, and Θ is Heaviside step function. The position vector of the j 'th robot at the timestamp t is given by

$$\hat{r}_j(t) = x_j(t)\hat{x} + y_j(t)\hat{y}, \quad (8)$$

where \hat{x} and \hat{y} are unit vectors. The sustainability parameter $\chi_4(\tau; a)$ can be evaluated as the variance of $Q(t, \tau; a)$ over the time interval:

$$\chi_4(\tau; a) = N \text{Var}_t(Q(t, \tau; a)). \quad (9)$$

Then, according to Ref. [26],

$$\tau^* = \max_{\tau} \chi_4(\tau; a) \quad (10)$$

is a characteristic trapping time for the robot around a given position, see Figure 3(e).

D. 3D correlation statistics

Two-dimensional pair correlation [28] quantifies the probability per unit area (normalized by the area density ρ) of finding another robot at the location (x, y) away from the reference robot, Figure 3(f):

$$g(x, y) = \frac{A}{N_{\text{total}}} \left\langle \sum_{j \neq i} \delta [x\hat{x}_i + y\hat{y}_i - (\hat{r}_i - \hat{r}_j)] \right\rangle_i, \quad (11)$$

where δ is pseudo Dirac function ($\delta(0) = 1$ instead of ∞), N_{total} is the total number of robots, A is a scaling factor, \hat{r}_i is the radius-vector of i 'th robot center, \hat{x}_i and \hat{y}_i are the transverse and longitudinal axes with respect to \hat{r}_i , and $\langle \dots \rangle_i$ represents averaging over all robots. The physical meaning of this quality is the following. If the centers of robots cannot locate at a certain distance from each other (e.g., at a distance closer than the robot's diameter), $g(x, y)$ will tend to zero, while at characteristic distances between robots packed in typical clusters, crystalline lattice, etc., the values of $g(x, y)$ will be finite, as shown in Figure 3(f). A similar picture has been obtained experimentally for self-rotating robots [29].

Orientation correlation function [28] reflects the orientation dependencies between the robots:

$$C_\theta(x, y) = \langle (\hat{y}_i \cdot \hat{y}_j) \delta [x\hat{x}_i + y\hat{y}_i - (\hat{r}_i - \hat{r}_j)] \rangle_{ij}, \quad (12)$$

where $\langle \dots \rangle_{ij}$ represents averaging over all possible pairs. According to the formula, the C_θ parameter tend to have higher values when robots at location (x, y) are oriented in the same direction as the reference robot. In the case of robots without a circular symmetry, such as Type-II Swarmodroids, this quantity characterizes spatial alignment of the robots.

Velocity correlation function [28] allows to capture velocity dependencies between the robots:

$$C_v(x, y) = \frac{\langle (\hat{v}_i \cdot \hat{v}_j) \delta [x\hat{x}_i + y\hat{y}_i - (\hat{r}_i - \hat{r}_j)] \rangle_{ij}}{\langle \hat{v}_i \cdot \hat{v}_i \rangle_i}, \quad (13)$$

where \hat{v}_i is the velocity vector of i 'th robot. Such a quantity will reach its maximal value when the velocity directions of all robots are aligned, and can be useful in visualizing flocking and other alignment phenomena.

V. DYNAMICS OF INDIVIDUAL ROBOTS

To engineer collective behavior of robotic swarms or study their physics, one needs a knowledge of the parameters corresponding to individual robots. To this end, we perform a detailed characterization of individual Swarmodroids addressing their angular (for Type-I) and linear (for Type-II) velocities, vibration spectra, and the evolution of these parameters upon changing the PWM rate.

To measure the vibration spectra of robots, we use IMVVP-4200 accelerometer working at the sampling frequency $f_s = 10$ kHz. To guarantee a reliable fastening, the accelerometer is screwed to a modified cap incorporating an accelerometer-shaped hole. During the vibration measurements, Swarmodroids are attached to the table with the help of two-sided adhesive tape to limit the magnitude of their oscillations and enhance the quality of measurements. We obtain time series of the vibration amplitude with the help of LabVIEW software package. Then, we apply Fourier transform to process the extracted time series and evaluate a vibration spectrum of each robot.

Figure 4(a) demonstrates vibration spectra of four different Type-I Swarmodroids, all working at PWM = 20%. The spectra feature the presence of a pronounced peak corresponding to the main mode with a frequency around $f_0 \approx 250$ Hz for PWM = 20% surrounded by much lower peaks of other modes. It is seen that the main frequency f_0 remains nearly the same for all considered robots, while the structure of other peaks may considerably fluctuate. Figure 4(b) demonstrates such spectra for a single Type-I Swarmodroid working at different PWM rates from 10% to 50%, respectively. When PWM is increased, the frequency of this main mode shifts linearly from $f_0 \approx 180$ Hz for PWM = 10% towards higher values, up to $f_0 \approx 385$ Hz for PWM = 50%. Thus, the swarm can be approximately described with a single characteristic vibration frequency f_0 , which linearly depends on the PWM rate.

Experimentally measured angular velocities ω_i of seven Type-I Swarmodroids at different PWM levels are shown in Fig. 4(c). It is seen that the velocities grow monotonically for all considered robots upon increasing the PWM rate. However, some dispersion of angular velocity values is observed at low PWM = 10% and PWM = 20%, which becomes considerable for larger PWM values. Figure 4(e) demonstrates velocities v_i of seven Type-II Swarmodroids in the same manner. Similar to the self-rotating robots of Fig. 4(c), self-propelled ones demonstrate a monotonic growth of velocities with increasing PWM level. The velocities v_i and angular velocities ω_i for PWM = 20% are shown in Figure 4(d,f), respectively, to illustrate the stability of these parameters. The maximal linear velocity error after averaging over five different realizations is about ± 2.5 cm/s, while the maximal deviation from the mean angular velocity is about ± 1.5 revolutions per second.

VI. COMPARISON WITH DIFFERENT ROBOTIC ACTIVE MATTER PLATFORMS

In this Section, we analyze different wheeled robots and bristle-bots with characteristics summarized in Table 5 to outline their areas of applicability and establish a certain region for Swarmodroid.

Many experimental studies of robotic swarm physics

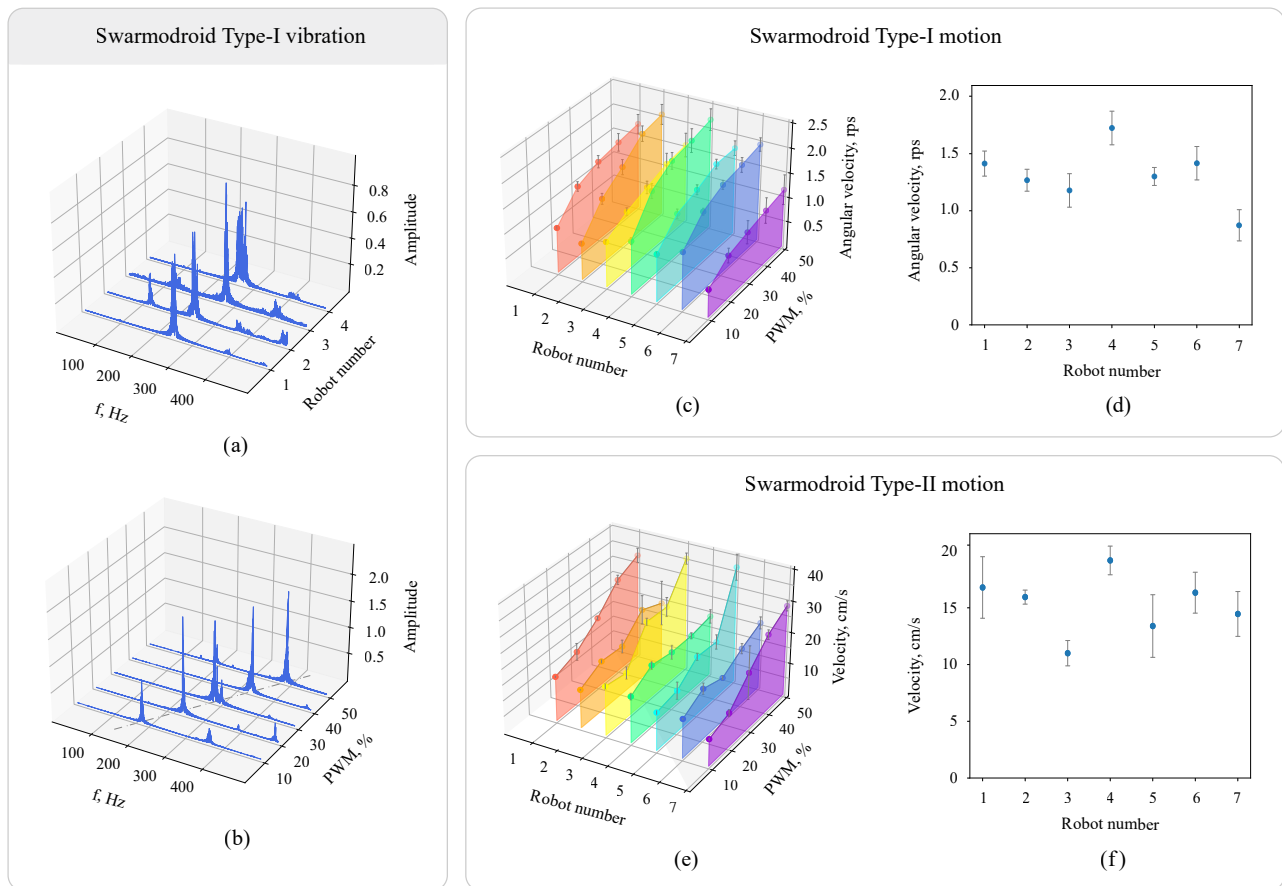


Figure 4. Properties of individual (a-d) Type-I (circular, self-rotating) and (e-f) Type-II (stadium-shaped, self-propelled) Swarmodroids. (a) Vibration spectra of four different Type-I robots. (b) Vibration spectra of a single Type-I robot at different PWM levels from 10% to 50% with the step 10%. (c) Angular velocities ω_i as functions of PWM level for seven different Type-I Swarmodroids. The values are obtained by repeating the measurement five times for each robot, and error bars denote the dispersion. (d) Angular velocity ω_i averaged over five realizations for each of seven Type-I Swarmodroids at PWM = 20%. (e) The same as Panel (c), but for linear velocities v_i of seven Type-II Swarmodroids at different PWM levels. (f) Linear velocity v_i averaged over five realizations for each robot at PWM = 20%.

employ HEXBUGS[®], the simplest commercial bristle-bots [30] distributed as toys. The examples include a study of boundary-controlled swarm dynamics [2, 3], the emulation of traffic jams [10] and financial price dynamics [12], experimental studies of polarized wall currents of self-propelled particles [31], the dynamics of a single robot in a parabolic potential [32], and other studies. The strong and weak sides of this platform come from the same basis – its extreme simplicity. Indeed, such a simple structure and mass-production render HEXBUGS[®] the most affordable platform to perform active matter studies requiring tens or even hundreds of robots. However, such a simplicity considerably limits the use of these bristle-bots which were initially designed as a toy and not as a scientific instrument. Indeed, HEXBUGS[®] cannot be turned on and off simultaneously via a remote control and need to be placed in the system one by one, which may affect the physics of the swarm. Moreover, their motion characteristics (governed by the shape of bristles) and motor vibration patterns cannot be controlled

as well. Thus, the only left degree of freedom to address novel physics is changing the shape of HEXBUGS[®] bodies or append them with additional elements. For example, HEXBUGS[®] have been supplied with magnets to demonstrate a magnetotaxis inspired by biological systems [33] and turned into chiral self-rotating matter by merging two HEXBUG[®] bristle-bots together to study the emergence of robust edge currents [11].

As a result, when more specific functionalities are required, many groups turn to their own hardware platforms. Such robots range from rather simple BBots applied to study the swirling and swarming behavior in Ref. [16] to more advanced BOBbots including magnets to introduce the attraction between the robots and wireless chargers to simplify their maintenance [6]. There are also several uncommon designs ranging from an extra-small 5 milligram bristle-bot [42] to a bristless SurferBot – a vibrobot capable of moving on the surface of water [41]. However, the uniqueness of such robots complicates their reproduction by other research groups, and

Wheeled robots												
Platform	Release year	Size, cm	Mass, g	Linear motion velocity, cm/s	Rotation freq., rad/s	Processing software	Recognition technology	Programming control level	Activity control (on-the-go)	Shape versatility	Synchronized activation	Price, \$
Elisa-3	2013	5	39	60	-	SwisTrack	IR emitters	Medium	Yes	Yes	Yes	390
AMiR	2009	6.5	n/a	8.6	-	WhyCon	Markers	Medium	Yes	No	Yes	78
e-Puck 2	2009	7	150	15	n/a	IRIDA	Markers	High	Yes	No	Yes	1200
Colias	2014	4	28	35	-	custom	Markers	High	Yes	No	Yes	30
Alice	2000	2.2	5	4	-	custom	LED	High	Yes	Yes	Yes	n/a
Jasmine-III	2005	3	n/a	30	-	custom	n/a	Medium	Yes	No	Yes	130
Bristle-bots												
Hexbug	2007	4.3	7	40	-	custom	Coloured spots	No	No	No	No	5
BBots	2012	7.92	15.5	20	30	n/a	n/a	No	No	No	No	n/a
SurferBot	2022	5	2.6	10	-	imaqtool	Coloured dots	No	No	No	No	n/a
BOBbots	2021	6	60	4.8	1.9	n/a	n/a	Medium	Yes	No	Yes	n/a
Kilobot	2012	3.3	16	1	0.8	trackpy	Shape	Medium	Yes	No	Yes	14
Swarmdroid (c)	2022	5	21	-	6.3 - 12.6	AMPy	ArUco markers	Medium	Yes	Yes	Yes	11
Swarmdroid (s)	2022	8.5	23	5 - 40	-	AMPy	ArUco markers	Medium	Yes	Yes	Yes	11

Figure 5. Comparison of several wheeled robots [34–40] and bristle-bots [2, 6, 16, 17, 41], including Swarmdroid 1.0. Column "Size" contains the largest dimension of the robot. "Linear motion velocity" and "Rotation frequency" also show the maximal values. Column "Recognition technology" highlights the tools allowing to track the robot position. The most tracking algorithms are not provided as a part of the respective platforms. In the column "Programming control level", label "No" corresponds to the case of primitive robots, which could be turned on and off only manually, "Medium" denotes robots allowing remote control and velocity tuning, and label "High" is assigned to the robots having some sensors, for instance, IR transmitters and receivers for obstacle avoiding and programming interactions between the robots. "Shape versatility" and "Synchronized activation" note the possibility of changing the geometry of individual robots and simultaneously turning on and off all robots in the swarm, respectively.

hence limits further development of the results, in contrast to HEXBUG®-based platforms. Moreover, many of such custom robots demonstrate large fluctuations in their motion characteristics from robot to robot associated with their manual production.

Another widely used robots are Kilobots [17] which represent an example of a polished and powerful platform designed for conducting scientific experiments, in contrast to HEXBUGs®. Being able to communicate via optical channels with the help of light-emitting diodes, carrying a programmable microcontroller, and supplied with two vibration motors, they were applied to demonstrate self-organization in predefined shapes following local algorithms [14], emulate tissue morphogenesis [43], and in numerous other examples. However, by their design Kilobots move slowly and via discrete steps, thus being more suitable for hardware implementations of various cellular automata and other mathematical models rather than to study physics governed by mechanical interactions between robots, the formation of force chains, and other phenomena requiring robots to move at high speeds and collide. To the best of our knowledge, there

is a single example of faster-moving Kilobots (5 cm/s instead of 0.5 cm/s) supplied with additional 3D-printed tripods [13].

First compact swarm robotics platforms employed robots moving with the help of wheels, with two-wheeled robots being a minimal example. Compared to bristle-bots, such robots are typically much more complex (and, as a result, more expensive). In particular, each of the robots in Table 5 incorporates IR sensors and emitters for obstacle avoidance and coordination of the interaction between robots. Also, the considered platforms support installation of additional devices, including a video camera (e-puck2, Alice), accelerometers (Elisa-3, e-puck2), microphones (AMiR, e-puck2), ultrasound sensors (Colias), and RF modules (Elisa-3, Alice), etc. However, high prices limit the affordable number of robots in the swarm, and in the most mentioned papers experimental studies are performed with systems containing just three to 20 robots, which is much lower than in typical bristle-bot swarms.

Elisa-3 is an open-source platform [34] compatible with the state-of-the-art Arduino and incorporating a wide

range of sensors. The platform is also provided with docking station for contact charging. The swarms of four to 25 Elisa-3 robots have been used for development of distributed algorithms for dynamic task execution based on RF communication between the robots [44]. Colias [37] and AMiR [35] are relatively low-cost open-hardware robots frequently used in experimental realization of BEECLUST algorithm (inspired by the collective behavior of honeybees) with the help of a light or sound potential [37, 45]. Small-sized Jasmine [39] robots with open-source software and hardware are also commonly used to execute BEECLUST scenario [46]. Miniature and lightweight Alice robotic platform [38] outstands for its 10 hours of autonomous work. The swarm of 20 Alice robots emulating cockroach aggregation is considered in Ref. [47]. Finally, e-puck2 [36] represents the most complicated platform among the considered ones having a comprehensive set of sensors. However, it is rather used for educational tasks than in research because of its high price. Nevertheless, even a low number of e-puck2 robots demonstrate successful occlusion-based cargo transport requiring visual recognition of an object and a target without any communication between the robots [48].

VII. EXAMPLE STUDIES

In this Section, we consider two examples of swarms with various configurations of Swarmodroids: self-rotating Type-I and self-propelled Type-II. Both studies use the same PCBs, microcontroller firmware, and processing software, yet demonstrate completely different phenomena due to different designs of modular plastic bodies which can be quickly reconfigured. While the first example considers a possible application scenario, the second one represents a fundamental study in the areas of physics and traffic-related problems, highlighting the versatility of the developed platform.

Example study 1: Cargo transport by self-rotating robots

Cargo transport by robotic swarms is an important task addressed in various designs including bristlebots [3, 6], wheeled robots [48], and other platforms [49]. In the most representative cases, a transport of passive objects should be attainable only with a robotic swarm, while a single robot is unable to manage such a load. Several studies above report a cooperative transport of such cargoes at the scales from tens of centimeters [6] down to one millimeter [49]. At the same time, many of these works demonstrate experiments with cargoes comparable with individual robots in size [1], consider specific examples like cleaning up an arena from several obstacles by clinging them to the corners [3], or are limited by the numerical studies only [50].

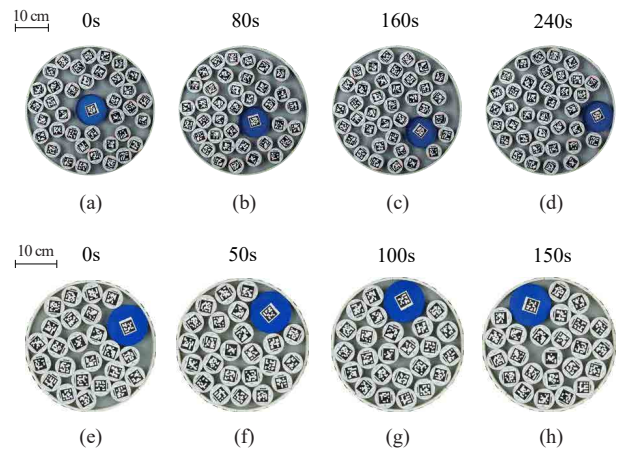


Figure 6. Collective cargo transport by a swarm of self-rotating Type-I Swarmodroids. (a)-(d): The process of cargo pushing from the center of the circular area to its boundary by the swarm consisting of 18 CW and 19 CCW robots. PWM rates at the shown timestamps are the following: (a) $\text{PWM}_{\text{CW,CCW}} = \{10\%, 10\%\}$, (b) $\text{PWM}_{\text{CW,CCW}} = \{10\%, 30\%\}$, (c) $\text{PWM}_{\text{CW,CCW}} = \{10\%, 45\%\}$, and (d) $\text{PWM}_{\text{CW,CCW}} = \{25\%, 10\%\}$. The boundary diameter is $D = 40$ cm and the packing density is $\Phi = 0.58$. (e)-(h): Directional cargo transport along the boundary by the swarm of 12 CW and 12 CCW robots working at the following PWM rates: (e) $\text{PWM}_{\text{CW,CCW}} = \{10\%, 10\%\}$, (f) $\text{PWM}_{\text{CW,CCW}} = \{10\%, 20\%\}$, (g) $\text{PWM}_{\text{CW,CCW}} = \{10\%, 35\%\}$, and (h) $\text{PWM}_{\text{CW,CCW}} = \{10\%, 45\%\}$. Robots are confined in a circular area with the diameter $D = 30$ cm and packing density $\Phi = 0.69$. The diameter of the blue-colored cargo is $d_{\text{cargo}} = 1.5d_{\text{robot}}$, and its mass is $m_{\text{cargo}} = 0.52m_{\text{robot}}$. Scale bars are 10 cm.

Here, we consider experimentally a chiral system consisting of self-rotating Type-I Swarmodroids pushing a passive object. The robots and test cargo ($D_{\text{cargo}} = 73$ mm and $m_{\text{cargo}} = 11$ g) are placed in a circular barrier with the inner diameter D , Figure 6. Angular velocities of the two subsets, clockwise (CW) and counter-clockwise (CCW) rotating robots, can be adjusted independently. This is implemented by tuning these subsets to the different command sets of IR signals transmitted by the remote. Thus, we can control the effective total chirality of the swarm by tuning the activity of CW and CCW robots on the go instead of changing the ratio of their numbers. This can be especially useful if one needs to conserve the number of robots during the experiment.

In the experiments, we initially set up the same PWM rate for CW and CCW robots $\text{PWM}_{\text{CW}} = \text{PWM}_{\text{CCW}} = 10\%$, and then increase PWM_{CCW} with 5% step every 20 seconds keeping the PWM_{CW} value equal to 10%. After PWM_{CCW} reaches 45%, we set again $\text{PWM}_{\text{CW}} = \text{PWM}_{\text{CCW}} = 10\%$ and repeat the measurements, but now changing PWM_{CW} in the same fashion. Along with PWM rates for CW and CCW robots, the swarm is also characterized by the packing density $0 < \Phi < 1$ defined as the ratio of the area covered by N robots S_{robots} to-

gether with the cargo S_{cargo} to the total area encircled by the boundary S_{barrier} :

$$\Phi = \frac{S_{\text{robots}} + S_{\text{cargo}}}{S_{\text{barrier}}} = \frac{\sum_{i=1}^N d^2 + d_{\text{cargo}}^2}{D^2} \quad (14)$$

We start with considering the swarm of 18 CW and 19 CCW robots confined in a boundary with the diameter $D = 40$ cm corresponding to the packing density $\Phi = 0.58$. An important point of the considered configuration is that the robots are far from jamming. Thus, the robots and cargo can move and change their relative locations. In this case, we observe directed transport of the cargo from the center of the area to its boundary, as shown in Figure 6(a-d). Possible mechanisms behind this effect may be related to a radial dependence of pressure caused by the active self-rotational behavior of individual robots and to a radial dependence of the local robot packing density in a barrier with curvature comparable to the size of individual robots.

In the second series of experiments, we consider a densely packed system of 12 CW and 12 CCW robots in the boundary with $D = 30$ cm corresponding to $\Phi = 0.69$. This system is close to jammed state and rigid. As a result, the robots and cargo cannot considerably move with respect to their neighbors and only slightly fluctuate around their locations. Thus, the cargo cannot be moved from the center to the edge like in Figure 6(a-d), and keeps its radial location. However, such a system demonstrates the rotation of a robotic swarm as a whole, which can be utilized for cargo transport along the boundary, as shown in Figure 6(e-h). In contrast to the first case, the cargo moves along the boundary in the direction defined by the total chirality of the system.

Example study 2: Jamming of self-propelled robots in a bottleneck

One of the interesting phenomena studied in swarms of self-propelled particles is the jamming transition from a mobile particle collective to a rigid glass-like state (without forming a crystal lattice) [27, 51–53]. The transition to a congested state takes place when the system packing density exceeds the critical value. However, if there are any obstacles (or bottlenecks), the formation of a jam by moving particles can occur locally, even if the system is below the critical density. Such a local phase transition between a free flow of a robotic swarm and the jammed state was considered for a system of HEXBUG® bristlebots moving at a fixed velocity [10]. In this example, the switching between the phases was achieved simply by changing the number of robots. In Ref. [12], a narrow opening connecting two chambers with HEXBUGs® allowed emulating financial price fluctuations. However, such a local traffic jam formation in a bottleneck has not been explored experimentally in the case when the velocity of robots is changed.

In this study, we consider a system of self-propelled Type-II Swarmodroids confined in a racetrack having a bottleneck, Figure 7(a). The track is implemented as a pair of 3D-printed non-concentric rings with inner diameters $D_1 = 59$ cm and $D_2 = 30$ cm. Their border widths are 3 cm and 1.5 cm, respectively. As variable parameters of the system, we consider the bottleneck width $h = \{50, 60, 67, 75\}$ mm, three levels of PWM = {10%, 20%, 30%}, and different total numbers of robots in the swarm $N = \{10, 12, 15, 17, 20\}$. For each set of parameters, the motion of robots was recorded during 120 seconds with 50 fps framerate, and the results were averaged over four different realizations of the initial robots placement.

To study the motion of particles in this system quantitatively, we consider polar coordinates of each robot (ρ_i, φ_i) with respect to the center of a circular boundary in Figure 7(a) and evaluate a temporal evolution of the parameter Ψ defined as

$$\Psi(k) = \sum_{i=2}^k \langle \varphi_i - \varphi_{i-1} \rangle \quad (15)$$

where $\langle \varphi_i - \varphi_{i-1} \rangle$ is a polar angle shift between the i 'th and the $(i-1)$ 'st frame averaged over N robots, and k is the number of a current frame. Polar angle values have been extracted for every fifth frame (i.e., time step is 0.1 s considering a 50 fps video). The linear dependence of $|\Psi|(t)$ corresponds to a free (ballistic) flow of robots along a circular trajectory, while the plateau in $|\Psi|(t)$ indicates jamming. During the video processing, we discard the records in which a robotic swarm becomes stuck outside the bottleneck (e.g., upon a collision of two groups of robots circulating in the opposite directions) or the whole swarm accidentally changes the direction of its motion. Both these cases lead to a plateau in $|\Psi|(t)$ dependence or even a decrease in $|\Psi|(t)$. However, they do not correspond to a jamming in the bottleneck, and thus are out of the scope of the present study.

The obtained experimental results are shown in Fig. 7. A significant difference in the dynamics is observed between sparse systems continuously moving along the boundary [Fig. 7(b,c)] and densely packed systems featuring jam formation [Fig. 7(d-f)]. In most cases, especially for sparse systems with $N = 10, 12$, an increase in the bottleneck width h is accompanied by a decrease in the average swarm mobility. The reason behind such a behavior may be the following. In the case of a small width $h = 50$ mm, the robots pass through the bottleneck one at a time, while larger values of h allow a pair of robots moving in parallel to reach the bottleneck simultaneously and form a jam there. Then, upon further increase in h , two robots may freely pass the bottleneck, etc.

Also, the averaged mobility for certain numbers of robots N and bottleneck width values h possesses a non-monotonous dependence on PWM rates. For example, in most of the cases the intermediate value of PWM = 20%

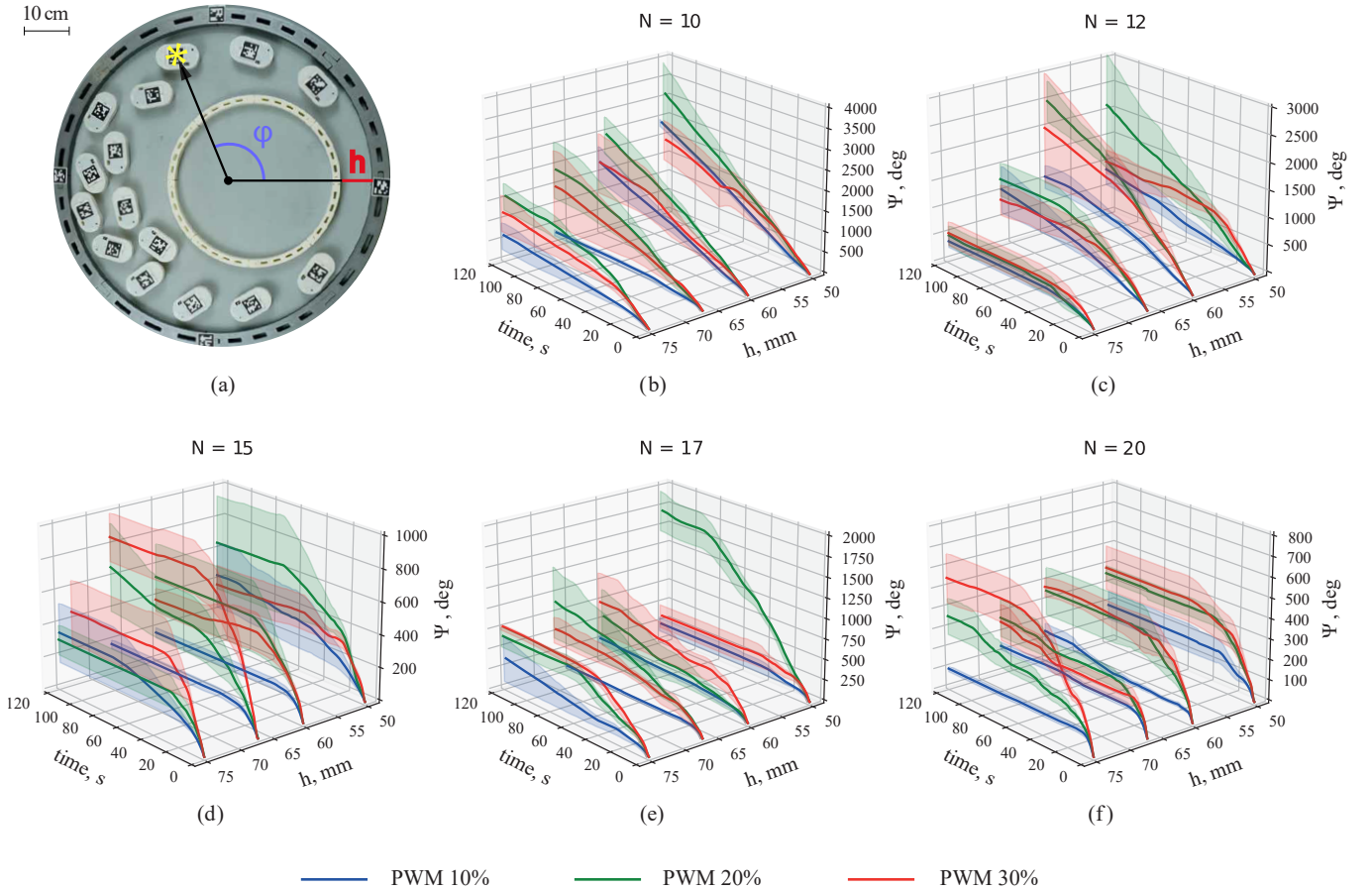


Figure 7. (a) The photo of experimental setup consisting of 15 self-propelled Type-II Swarmodroids confined between two circular barriers. Red line denotes the width of the bottleneck h . The plots in panels (b)-(f) represent time dependencies of parameter Ψ Eq. (15) for different values of bottleneck width h as well as different activity rates for $N = 10, 12, 15, 17,$ and 20 robots, respectively. Different curve colors correspond to the following PWM levels: 10% (blue), 20% (green), and 30% (red).

corresponds to the free flow or jamming occurring later than in swarms moving with $PWM = 30\%$, Figure 7(b-f). However, in some cases (e.g., the system with parameters $N = 15$ and $h = 70$ mm or $N = 20$ and $h = 75$ mm) the robots moving with $PWM = 30\%$ feature higher mobility, as seen in Figure 7(d,f).

Majority of experiments demonstrate transition from the free flowing robots to jammed ones only, however some realizations also feature an inverse phenomena, un-jamming. Such an unclogging is observed, for instance, for the following set of parameters: $\{N; h; PWM\} = \{10; 50; 30\}$, $\{15, 70, 20\}$, and $\{20; 60; 10\}$, respectively.

OUTLOOK

A comparison of different platforms for realizing swarms of extremely simple robots shows that, despite demonstrating certain advantages in specific areas, such platforms still lack versatility and are limited in their application scenarios. To standardize this area and enhance the reproducibility of results, in the present Ar-

ticle we introduced an open-source Swarmodroid platform featuring bristle-bots with a remote IR control, a set of 3D-printable plastic parts to reconfigure them for different application scenarios, and software capable of automatic extraction of various quantities characterizing the behavior of the swarm. We supply our manuscript with two review sections: one comparing different robotic platforms and the other introducing basic quantities describing swarm dynamics.

As demonstrated by studies of individual robots, they can be described by a characteristic vibration frequency f_0 that slightly deviates between different robots and linearly grows from $f_0 \approx 180$ Hz to $f_0 \approx 380$ Hz with an increase in the pulse modulation width of the vibration motor from $PWM = 10\%$ to $PWM = 50\%$. Self-rotation angular velocities of Type-I Swarmodroids and motion velocities of the self-propelled Type-II Swarmodroids grow monotonically upon such an increase in PWM as well, which allows controlling the dynamics of the swarm on the go by changing the PWM rate with the help of IR remote.

Further experiments with swarms consisting of tens of

Swarmodroids outline two groups of use cases for the platform.

The first group includes the development of applications of such simple robots, e.g. implementation of collective functions. As an example, we demonstrate cargo pushing from the center of the area filled with robots to its boundary and cargo transport along a circular boundary. This study extends recent illustrations of cargo transport by self-propelled robots [48] and microparticles [49], as we use self-rotating robots with a completely different motion pattern. Such self-rotating objects have been implemented at different scales ranging from several centimeters [11] to millimeters [54, 55] to even microscale [56], highlighting the relevance of such a motion pattern of individual particles. Within the applied area, we highlight the following ideas that are worth examination:

- Developing robot bodies with specific shapes and properties (water-resistant, spherical, etc.) to use individual Swarmodroids as a cheap and compact platform to carry various sensors. Such robots can be used, for example, in pipe inspection [57, 58], or to navigate the surface of water [41, 59] and perform its monitoring.
- Inspection of obstructions, hazardous environments, space infrastructure [60], and geological objects by swarms of robots equipped with sensors and transmitters in cases when required robot sizes are strictly limited and incompatible with the use of cameras, LIDARs, on-board computers, etc., or when the robots are likely to be destroyed, and minimizing their cost is important.
- Engineering different self-organization patterns in order to realize the shape-morphing matter [5, 43, 61–63]. Within our platform, there are two possible ways to achieve such a functionality: by implementing time-dependent profiles of PWM rate and by studying different body shapes like those illustrated in Figure 8.
- Realizing various collective algorithms to increase the efficiency of large robotic swarms, such as a liquid-mimicking behaviour studied in Ref. [64] which allows enhancing obstacle avoidance by robotic swarms.
- Implementing universal grips working on jamming transition in the swarms (similar to those of Figure 7) or able to rotate objects of arbitrary shape based on the effect demonstrated in Figure 6(e-h). Such devices were demonstrated considering jamming in a passive granular media [65]. One can start with Swarmodroids placed in a flexible barrier similar to those of Refs. [2, 3], but at higher densities compared to the mentioned papers.

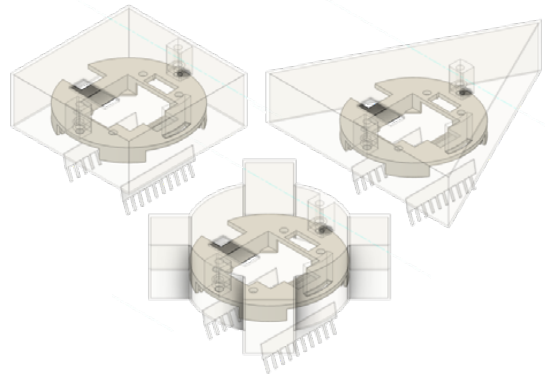


Figure 8. Renders of various Swarmodroid body designs which can be implemented by replacing the upper cap only and may result in different collective behavior.

The second scenario is focused on fundamental studies in the areas of physics, biology, and transportation, and is illustrated by the study of jamming in the bottleneck.

- In physics, such robotic swarms can be used as educational toy models for various phenomena [66], demonstrations of novel theoretical predictions which cannot be implemented in natural materials yet [67], or even as a source of novel experimental data [15]. Regarding our platform, we propose to tackle the problems that require velocity variation or specific shapes of robotic bodies, such as various self-organization scenarios [68].
- Robotic swarms are often used to mimic the behaviour strategies of various biological systems, such as worm blobs [69] or insect colonies [70–72].
- Many problems in pedestrian dynamics are modelled with the help of particle swarms [73, 74], including hydrodynamic approaches [75, 76]. In this light, our platform can be used to consider phenomena like the jamming of pedestrians in narrow exits [77, 78], emulate interactions governed by simple rules [79], and study the formation of collective structures [80]. Besides, such robotic swarms can be applied to experimentally implement various simplified traffic models [81].

Finally, we would like to outline the following key directions of further development of the Swarmodroid platform:

- Introducing steering ability by developing bodies supporting two considerably different vibration modes [82] or incorporating the second vibration motor [17].
- Implementing a simultaneous charging of many robots via external contacts like the ones used in Kilobots [17], and ultimately, applying wireless power transfer [6, 83, 84].

- Removing screws that accompany magnetic latches in the present revision and introducing additional connectors to enhance reconfigurability.

We encourage all members of the community to introduce their ideas and develop modifications of the proposed Swarmodroid platform.

ACKNOWLEDGEMENTS

The authors acknowledge valuable discussions with Anton Souslov, Dmitry Filonov, Denis Butusov, Evgenii Svechnikov, and Egor Kretov. The work is partially supported by School of Physics and Engineering, ITMO University (RPMA grant). The studies of collective effects in robotic swarms were partially supported by the Russian

Science Foundation (grant No. 20-19-00491).

AUTHOR CONTRIBUTIONS

A.D. designed the printed circuit boards and developed firmware. A.R. and A.M. designed bodies and optimized bristles. V.P. and M.B. developed AMPy package. D.S., V.S., M.B., and T.K. performed studies of individual robots. O.B. measured discharge characteristics. A.R. performed studies of collective effects. A.R. and N.O. compared robotic platforms. V.P. and N.O. reviewed characteristic quantities describing active matter systems. E.P., A.R., A.D., and O.B. soldered PCBs and assembled robots. N.O. put forward the idea and supervised the project. All authors contributed to the manuscript preparation, data processing, and discussion of results.

-
- [1] Shuguang Li, Richa Batra, David Brown, Hyun-Dong Chang, Nikhil Ranganathan, Chuck Hoberman, Daniela Rus, and Hod Lipson, “Particle robotics based on statistical mechanics of loosely coupled components,” *Nature* **567**, 361–365 (2019).
- [2] A. Deblais, T. Barois, T. Guerin, P. H. Delville, R. Vaudaine, J. S. Lintuvuori, J. F. Boudet, J. C. Baret, and H. Kellay, “Boundaries control collective dynamics of inertial self-propelled robots,” *Physical Review Letters* **120**, 188002 (2018).
- [3] J. F. Boudet, J. Lintuvuori, C. Lacouture, T. Barois, A. Deblais, K. Xie, S. Cassagnere, B. Tregon, D. B. Brückner, J. C. Baret, and H. Kellay, “From collections of independent, mindless robots to flexible, mobile, and directional superstructures,” *Science Robotics* **6**, abd0272 (2021).
- [4] William Savoie, Thomas A Berrueta, Zachary Jackson, Ana Pervan, Ross Warkentin, Shengkai Li, Todd D Murphey, Kurt Wiesenfeld, and Daniel I Goldman, “A robot made of robots: Emergent transport and control of a smarticle ensemble,” *Science Robotics* **4**, eaax4316 (2019).
- [5] Pavel Chvykov, Thomas A Berrueta, Akash Vardhan, William Savoie, Alexander Samland, Todd D Murphey, Kurt Wiesenfeld, Daniel I Goldman, and Jeremy L England, “Low rattling: A predictive principle for self-organization in active collectives,” *Science* **371**, 90–95 (2021).
- [6] Shengkai Li, Bahnisikha Dutta, Sarah Cannon, Joshua J Daymude, Ram Avinery, Enes Aydin, Andréa W Richa, Daniel I Goldman, and Dana Randall, “Programming active cohesive granular matter with mechanically induced phase changes,” *Science Advances* **7**, eabe8494 (2021).
- [7] Wenzhuo Yu, Haisong Lin, Yilian Wang, Xu He, Nathan Chen, Kevin Sun, Darren Lo, Brian Cheng, Christopher Yeung, Jiawei Tan, Dino Di Carlo, and Sam Emaminejad, “A ferrobotic system for automated microfluidic logistics,” *Science Robotics* **5**, eaba4411 (2020).
- [8] Yulei Fu, Hengao Yu, Xinli Zhang, Paolo Malgaretti, Vimal Kishore, and Wendong Wang, “Microscopic swarms: From active matter physics to biomedical and environmental applications,” *Micromachines* **13**, 295 (2022).
- [9] Wanyuan Li, Changjin Wu, Ze Xiong, Chaowei Liang, Ziyi Li, Baiyao Liu, Qinyi Cao, Jizhuang Wang, Jinyao Tang, and Dan Li, “Self-driven magnetorobots for recyclable and scalable micro/nanoplastic removal from non-marine waters,” *Science Advances* **8**, eade1731 (2022).
- [10] Thomas Barois, Jean-François Boudet, Nicolas Lanchon, Juho S. Lintuvuori, and Hamid Kellay, “Characterization and control of a bottleneck-induced traffic-jam transition for self-propelled particles in a track,” *Physical Review E* **99**, 052605 (2019).
- [11] Xiang Yang, Chenyang Ren, Kangjun Cheng, and H. P. Zhang, “Robust boundary flow in chiral active fluid,” *Physical Review E* **101**, 022603 (2020).
- [12] G A Patterson, D Sornette, and D R Parisi, “Properties of balanced flows with bottlenecks: Common stylized facts in finance and vibration-driven vehicles,” *Physical Review E* **101**, 042302 (2020).
- [13] Matan Yah Ben Zion, Jeremy Fersula, Nicolas Bredeche, and Olivier Dauchot, “Morphological computation and decentralized learning in a swarm of sterically interacting robots,” *Science Robotics* **8**, eabo6140 (2023).
- [14] Michael Rubenstein, Alejandro Cornejo, and Radhika Nagpal, “Programmable self-assembly in a thousand-robot swarm,” *Science* **345**, 795–799 (2014).
- [15] Jean François Boudet, Julie Jagielka, Thomas Guerin, Thomas Barois, Fabio Pistolesi, and Hamid Kellay, “Effective temperature and dissipation of a gas of active particles probed by the vibrations of a flexible membrane,” *Physical Review Research* **4**, L042006 (2022).
- [16] L. Giomi, N. Hawley-Weld, and L. Mahadevan, “Swarming, swirling and stasis in sequestered bristle-bots,” *Proceedings of the Royal Society A: Mathematical, Physical and Engineering Sciences* **469**, 20120637 (2013).
- [17] Michael Rubenstein, Christian Ahler, and Radhika Nagpal, “Kilobot: A low cost scalable robot system for col-

- lective behaviors,” in *2012 IEEE international conference on robotics and automation* (IEEE, 2012) pp. 3293–3298.
- [18] Free Software Foundation, GNU General Public License Version 3 (GPLv3), <https://www.gnu.org/licenses/gpl-3.0.en.html>, accessed 22 May 2023.
- [19] Vadim Porvatov, Alina Rozenblit, Alexey Dmitriev, Oleg Burmistrov, Daria Petrova, Georgy Gritsenko, Ekaterina Puhtina, Egor Kretov, Dmitry Filonov, Anton Souslov, and Nikita Olekhno, “Optimizing self-rotating bristlebots for active matter implementation with robotic swarms,” *Journal of Physics: Conference Series* **2086**, 012202 (2021).
- [20] “Remote control IR receiver/decoder,” Application Note AN-1184, Renesas Electronics Corporation, <https://www.renesas.com/us/en/document/apn/1184-remote-control-ir-receiver-decoder>, accessed 22 May 2023.
- [21] See Supplemental Material at [URL] for (i) power consumption of robots and battery characterization; (ii) algorithms of the robot firmware; (iii) firmware reference.
- [22] “ATTiny13/ATTiny13V: 8-bit AVR microcontroller with 1K bytes in-system programmable flash,” Datasheet, Rev. 2535J-AVR-08/10, Atmel Corporation, <https://ww1.microchip.com/downloads/en/development/doc2535.pdf>, accessed 22 May 2023.
- [23] Sebastian Bindgen, Frank Bossler, Jens Allard, and Erin Koos, “Connecting particle clustering and rheology in attractive particle networks,” *Soft Matter* **16**, 8380–8393 (2020).
- [24] Davide Breoni, Michael Schmiedeberg, and Hartmut Löwen, “Active Brownian and inertial particles in disordered environments: Short-time expansion of the mean-square displacement,” *Physical Review E* **102**, 062604 (2020).
- [25] Katherine J. Strandburg, *Bond-orientational order in condensed matter systems* (Springer Science & Business Media, 1992).
- [26] Gao Wang, Trung V. Phan, Shengkai Li, Michael Wombacher, Junle Qu, Yan Peng, Guo Chen, Daniel I. Goldman, Simon A. Levin, Robert H. Austin, and Liyu Liu, “Emergent field-driven robot swarm states,” *Physical Review Letters* **126**, 108002 (2021).
- [27] Aaron S Keys, Adam R Abate, Sharon C Glotzer, and Douglas J Durian, “Measurement of growing dynamical length scales and prediction of the jamming transition in a granular material,” *Nature Physics* **3**, 260–264 (2007).
- [28] H. P. Zhang, Avraham Be’er, E.-L. Florin, and Harry L. Swinney, “Collective motion and density fluctuations in bacterial colonies,” *Proceedings of the National Academy of Sciences* **107**, 13626–13630 (2010).
- [29] Alexey Dmitriev, Alina Rozenblit, Vadim Porvatov, Anastasia Molodtsova, Ekaterina Puhtina, Oleg Burmistrov, Dmitry Filonov, Anton Souslov, and Nikita Olekhno, “Statistical correlations in active matter based on robotic swarms,” in *2021 International Conference Engineering and Telecommunication (En&T)* (IEEE, 2021) pp. 1–3.
- [30] Spin Master, “HEXBUG Micro Robotic Creatures,” Accessed 22 May 2023.
- [31] Thomas Barois, Jean-François Boudet, Juho S Lintuvuori, and Hamid Kellay, “Sorting and extraction of self-propelled chiral particles by polarized wall currents,” *Physical Review Letters* **125**, 238003 (2020).
- [32] Olivier Dauchot and Vincent Démery, “Dynamics of a self-propelled particle in a harmonic trap,” *Physical Review Letters* **122**, 068002 (2019).
- [33] Néstor Sepúlveda, Francisca Guzmán-Lastra, Miguel Carrasco, Bernardo González, Eugenio Hamm, and Andrés Concha, “Bioinspired magnetic active matter and the physical limits of magnetotaxis,” arXiv:2111.04889 (2021).
- [34] GCTronic, Elisa-3, <https://www.gctronic.com/doc/index.php/Elisa-3>, accessed 22 May 2023.
- [35] Farshad Arvin, Khairulmizam Samsudin, Abdul Rahman Ramli, *et al.*, “Development of a miniature robot for swarm robotic application,” *International Journal of Computer and Electrical Engineering* **1**, 436–442 (2009).
- [36] GCTronic, e-puck2, <https://www.gctronic.com/doc/index.php/e-puck2>, accessed 22 May 2023.
- [37] Farshad Arvin, John Murray, Chun Zhang, and Shigang Yue, “Colias: An autonomous micro robot for swarm robotic applications,” *International Journal of Advanced Robotic Systems* **11**, 113 (2014).
- [38] Gilles Caprari, Thomas Estier, and Roland Siegwart, “Fascination of down scaling—Alice the sugar cube robot,” in *IEEE International Conference on Robotics and Automation (ICRA 2000): Workshop on Mobile Micro-Robots* (2000).
- [39] Jasmine: swarm robot platform, <http://www.swarmrobot.org>, accessed 22 May 2023.
- [40] Justin Y Kim, Tyler Colaco, Zendai Kashino, Goldie Nejat, and Beno Benhabib, “mROBerTO: A modular millirobot for swarm-behavior studies,” in *2016 IEEE/RSJ International Conference on Intelligent Robots and Systems (IROS)* (IEEE, 2016) pp. 2109–2114.
- [41] Eugene Rhee, Robert Hunt, Stuart J Thomson, and Daniel M Harris, “SurferBot: a wave-propelled aquatic vibrobot,” *Bioinspiration & Biomimetics* **17**, 055001 (2022).
- [42] DeaGyu Kim, Zhijian Hao, Jun Ueda, and Azadeh Ansari, “A 5 mg micro-bristle-bot fabricated by two-photon lithography,” *Journal of Micromechanics and Microengineering* **29**, 105006 (2019).
- [43] Ivica Slavkov, Daniel Carrillo-Zapata, Noemi Carranza, Xavier Diego, Fredrik Jansson, J Kaandorp, Sabine Hauert, and James Sharpe, “Morphogenesis in robot swarms,” *Science Robotics* **3**, eaau9178 (2018).
- [44] Rafael Mathias de Mendonça, Nadia Nedjah, and Luiza de Macedo Mourelle, “Efficient distributed algorithm of dynamic task assignment for swarm robotics,” *Neurocomputing* **172**, 345–355 (2016).
- [45] Farshad Arvin, Ali Emre Turgut, Farhad Bazyari, Kutluk Bilge Arikan, Nicola Bellotto, and Shigang Yue, “ Cue-based aggregation with a mobile robot swarm: a novel fuzzy-based method,” *Adaptive Behavior* **22**, 189–206 (2014).
- [46] Thomas Schmickl, Ronald Thenius, Christoph Moeslinger, Gerald Radspieler, Serge Kernbach, Marc Szymanski, and Karl Crailsheim, “Get in touch: cooperative decision making based on robot-to-robot collisions,” *Autonomous Agents and Multi-Agent Systems* **18**, 133–155 (2009).
- [47] Simon Garnier, Christian Jost, Jacques Gautrais, Masoud Asadpour, Gilles Caprari, Raphaël Jeanson, Anne Grimal, and Guy Theraulaz, “The embodiment of cockroach aggregation behavior in a group of micro-robots,” *Artificial life* **14**, 387–408 (2008).

- [48] Jianing Chen, Melvin Gauci, Wei Li, Andreas Kolling, and Roderich Groß, “Occlusion-based cooperative transport with a swarm of miniature mobile robots,” *IEEE Transactions on Robotics* **31**, 307–321 (2015).
- [49] Gaurav Gardi, Steven Ceron, Wendong Wang, Kirstin Petersen, and Metin Sitti, “Microrobot collectives with reconfigurable morphologies, behaviors, and functions,” *Nature Communications* **13**, 2239 (2022).
- [50] Qing Yang, Huan Liang, Rui Liu, Ke Chen, Fangfu Ye, and Mingcheng Yang, “Edge transport and self-assembly of passive objects in a chiral active fluid,” *Chinese Physics Letters* **38**, 128701 (2021).
- [51] M.E. Cates, J.P. Wittmer, J.-P. Bouchaud, and P. Claudin, “Jamming, force chains, and fragile matter,” *Physical Review Letters* **81**, 1841 (1998).
- [52] Simon Garcia, Edouard Hannezo, Jens Elgeti, Jean-François Joanny, Pascal Silberzan, and Nir S. Gov, “Physics of active jamming during collective cellular motion in a monolayer,” *Proceedings of the National Academy of Sciences* **112**, 15314–15319 (2015).
- [53] Rituparno Mandal, Pranab Jyoti Bhuyan, Pinaki Chaudhuri, Chandan Dasgupta, and Madan Rao, “Extreme active matter at high densities,” *Nature Communications* **11**, 2581 (2020).
- [54] Suk Chang, Vesselin Paunov, Dimiter Petsev, and O. Velev, “Remotely powered self-propelling particles and micropumps based on miniature diodes,” *Nature Materials* **6**, 235–240 (2007).
- [55] Piyush Kumar, Yi Zhang, Stephen J. Ebbens, and Xiubo Zhao, “3D inkjet printed self-propelled motors for micro-stirring,” *Journal of Colloid and Interface Science* **623**, 96–108 (2022).
- [56] Antoine Aubret, Mena Youssef, Stefano Sacanna, and J’er’emie Palacci, “Targeted assembly and synchronization of self-spinning microgears,” *Nature Physics* **14**, 1114–1118 (2018).
- [57] Zhelong Wang and Hong Gu, “A bristle-based pipeline robot for ill-constraint pipes,” *IEEE/ASME Transactions on Mechatronics* **13**, 383 – 392 (2008).
- [58] Felix Becker, Simon Börner, Tobias Kästner, Victor Lyosenko, Igor Zeidis, and Klaus Zimmermann, “Spy bristle bot—A vibration-driven robot for the inspection of pipelines,” in *58th Ilmenau Scientific Colloquium* (2014) pp. 1–7.
- [59] Yury L Karavaev, Anton V Klekovkin, Ivan S Mamaev, Valentin A Tenenev, and Evgeny V Vetchanin, “A simple physical model for control of a propellerless aquatic robot,” *Journal of Mechanisms and Robotics* **14**, 011007 (2022).
- [60] Bahar Haghighat, Johannes Boghaert, Ariel Ekblaw, and Radhika Nagpal, “A swarm robotic approach to inspection of 2.5D surfaces in orbit,” (2022) p. 8, available online: https://pure.rug.nl/ws/portalfiles/portal/639326471/2022_swarm.pdf.
- [61] Xiaoxing Xia, Christopher M Spadaccini, and Julia R Greer, “Responsive materials architected in space and time,” *Nature Reviews Materials* **7**, 683–701 (2022).
- [62] John W Romanishin, Kyle Gilpin, Sebastian Claici, and Daniela Rus, “3D M-Blocks: Self-reconfiguring robots capable of locomotion via pivoting in three dimensions,” in *2015 IEEE International Conference on Robotics and Automation (ICRA)* (IEEE, 2015) pp. 1925–1932.
- [63] Jonathan Daudelin, Gangyuan Jing, Tarik Tosun, Mark Yim, Hadas Kress-Gazit, and Mark Campbell, “An integrated system for perception-driven autonomy with modular robots,” *Science Robotics* **3**, eaat4983 (2018).
- [64] Shotaro Shibahara and Kenji Sawada, “Polygonal obstacle avoidance method for swarm robots via fluid dynamics,” *Artificial Life and Robotics* **28**, 435–447 (2023).
- [65] Eric Brown, Nicholas Rodenberg, John Amend, Annan Mozeika, Erik Steltz, Mitchell R Zakin, Hod Lipson, and Heinrich M Jaeger, “Universal robotic gripper based on the jamming of granular material,” *Proceedings of the National Academy of Sciences* **107**, 18809–18814 (2010).
- [66] Genevieve DiBari, Liliana Valle, Refilwe Tanah Bua, Lucas Cunningham, Eleanor Hort, Taylor Venenciano, and Janice Hudgings, “Using Hexbugs™ to model gas pressure and electrical conduction: A pandemic-inspired distance lab,” *American Journal of Physics* **90**, 817–825 (2022).
- [67] Martin Brandenbourger, Colin Scheibner, Jonas Veenstra, Vincenzo Vitelli, and Corentin Coulais, “Limit cycles turn active matter into robots,” arXiv:2108.08837 (2021).
- [68] Martin Lenz and Thomas A Witten, “Geometrical frustration yields fibre formation in self-assembly,” *Nature Physics* **13**, 1100–1104 (2017).
- [69] Yasemin Ozkan-Aydin and Daniel I. Goldman, “Self-reconfigurable multilegged robot swarms collectively accomplish challenging terradynamic tasks,” *Science Robotics* **6**, eabf1628 (2021).
- [70] Simon Garnier, Jacques Gautrais, Masoud Asadpour, Christian Jost, and Guy Theraulaz, “Self-organized aggregation triggers collective decision making in a group of cockroach-like robots,” *Adaptive Behavior* **17**, 109–133 (2009).
- [71] Justin Werfel, Kirstin Petersen, and Radhika Nagpal, “Designing collective behavior in a termite-inspired robot construction team,” *Science* **343**, 754–758 (2014).
- [72] S Ganga Prasath, Souvik Mandal, Fabio Giardina, Jordan Kennedy, Venkatesh N Murthy, and L Mahadevan, “Dynamics of cooperative excavation in ant and robot collectives,” *eLife* **11**, e79638 (2022).
- [73] Alexandre Nicolas, Marcelo Kuperman, Santiago Ibañez, Sebastián Bouzat, and Cécile Appert-Rolland, “Mechanical response of dense pedestrian crowds to the crossing of intruders,” *Scientific Reports* **9**, 105 (2019).
- [74] Iñaki Echeverría-Huarte, Alexandre Nicolas, Raúl Cruz Hidalgo, Angel Garcimartín, and Iker Zuriguel, “Spontaneous emergence of counterclockwise vortex motion in assemblies of pedestrians roaming within an enclosure,” *Scientific Reports* **12**, 2647 (2022).
- [75] Audrey Filella, François Nadal, Clément Sire, Eva Kanso, and Christophe Eloy, “Model of collective fish behavior with hydrodynamic interactions,” *Physical Review Letters* **120**, 198101 (2018).
- [76] Nicolas Bain and Denis Bartolo, “Dynamic response and hydrodynamics of polarized crowds,” *Science* **363**, 46–49 (2019).
- [77] Ioannis Karamouzas, Brian Skinner, and Stephen J. Guy, “Universal power law governing pedestrian interactions,” *Physical Review Letters* **113**, 238701 (2014).
- [78] Milad Haghani and Majid Sarvi, “Simulating pedestrian flow through narrow exits,” *Physics Letters A* **383**, 110–120 (2018).
- [79] Hisashi Murakami, Claudio Feliciani, Yuta Nishiyama, and Katsuhiko Nishinari, “Mutual anticipation can contribute to self-organization in human crowds,” *Science*

- Advances **7**, eabe7758 (2021).
- [80] Jesse L. Silverberg, Matthew Bierbaum, James P. Sethna, and Itai Cohen, “Collective motion of humans in mosh and circle pits at heavy metal concerts,” *Physical Review Letters* **110**, 228701 (2013).
 - [81] Takashi Nagatani, “The physics of traffic jams,” *Reports on Progress in Physics* **65**, 1331 (2002).
 - [82] Dila Türkmen and Merve Acer, “Development of a planar BBot using a single vibration motor,” in *2017 XXVI International Conference on Information, Communication and Automation Technologies (ICAT)* (IEEE, 2017) pp. 1–6.
 - [83] Farshad Arvin, Simon Watson, Ali Emre Turgut, Jose Espinosa, Tomáš Krajník, and Barry Lennox, “Perpetual robot swarm: long-term autonomy of mobile robots using on-the-fly inductive charging,” *Journal of Intelligent & Robotic Systems* **92**, 395–412 (2018).
 - [84] Takashi Ozaki, Norikazu Ohta, Tomohiko Jimbo, and Kanae Hamaguchi, “A wireless radiofrequency-powered insect-scale flapping-wing aerial vehicle,” *Nature Electronics* **4**, 845–852 (2021).

Supplementary Information: Swarmodroid 1.0: A Modular Bristle-Bot Platform for Robotic Active Matter Studies

CONTENTS

S1. Power consumption of robots and battery characterization	2
S2. Algorithm of the robot firmware	4
S2.1. The <code>main</code> procedure	4
S2.2. 8-bit Timer/Counter	7
S2.3. Pin change interrupt ISR	8
S3. Firmware reference	11
S3.1. Global variables	11
S3.2. Macro definitions: hardware-related constants	13
S3.3. Macro definitions: inline functions	14
S3.4. Macro definitions: definitions introduced for code clarity	17
S3.5. Remote control constants	19
S3.6. <code>measure_and_show_battery_idle_voltage</code> function	20
S3.7. <code>main</code> function	20
S3.8. Timer/Counter overflow interrupt service routine	24
S3.9. ADC conversion complete interrupt service routine	24
S3.10. Pin change interrupt service routine	25
References	29

S1 – POWER CONSUMPTION OF ROBOTS AND BATTERY CHARACTERIZATION

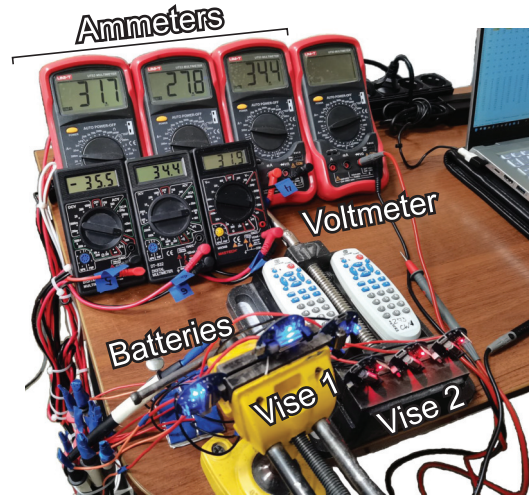


Figure S1: Experimental setup for discharging curves measurement. The setup includes three UT-53 and three DT-831 multimeters working as ammeters (labeled as Ammeters), one UT-53 multimeter working as a voltmeter (labeled as Voltmeter), and two vises (Vise 1 and Vise 2) that fasten six Swarmodroid boards supplied with extended wires. The batteries (labeled Batteries) are fastened separately onto the table.

To evaluate the maximum continuous operation time of the Swarmodroid, we perform experimental measurements of battery discharge curves for six randomly selected bots. Prior to the measurement, each printed circuit board (PCB) is extracted from the plastic body and fixed in a vise. To prevent the wires connecting the PCB and the battery from falling apart due to vibration, the batteries are fastened onto the table using a double-sided adhesive tape (see Fig. S1), and the 2 cm long wires that connect the PCB to the battery are extended by 10 – 30 cm. The bots firmware is alternated in a way that allows them continue vibrating even when the battery is discharged to the critical level of 3.3 V. The batteries are charged before the start of experiment until the charge current falls below 30 mA.

After charging, a voltmeter and an ammeter are attached in parallel and in series to the battery, respectively. To measure the current, we connect UNI-T UT-53 and Mastech DT-831 multimeters in the ammeter mode (0 – 200 mA range) in series between the positive battery output and the PCB. The voltage is measured periodically by connecting UT-53 multimeter in the voltmeter mode (0 – 20 VDC range) between the positive and negative outputs of each battery.

The values of voltages and currents are measured every 30 minutes for PCBs vibrating at PWM = 10% and PWM = 30%, and every 20 minutes in the case of PWM = 50%. The moment of total discharge is defined as a time when the voltage level reaches 2.4 V. The obtained results are shown in Fig. S2. It is seen that the discharge time monotonically depends on the PWM level. However, the dependence is nonlinear: discharge times for PWM = 10% [Fig. S2(a,d)] are approximately two times higher than for PWM = 20% [Fig. S2(b,e)], while the difference between PWM = 10% and PWM = 30% [Fig. S2(c,f)] is about 25%, highlighting that a collector engine needs more current on low rotation frequencies. Despite the incremental reduction of measured characteristics (caused by a simultaneous decrease in voltage and current), the robots were able to exhibit stable motility during the major part of working time. Average working times are 10 h 11 m, 5 h 11 m, and 3 h 45 m for PWM = 10%, 20%, and 30%, respectively.

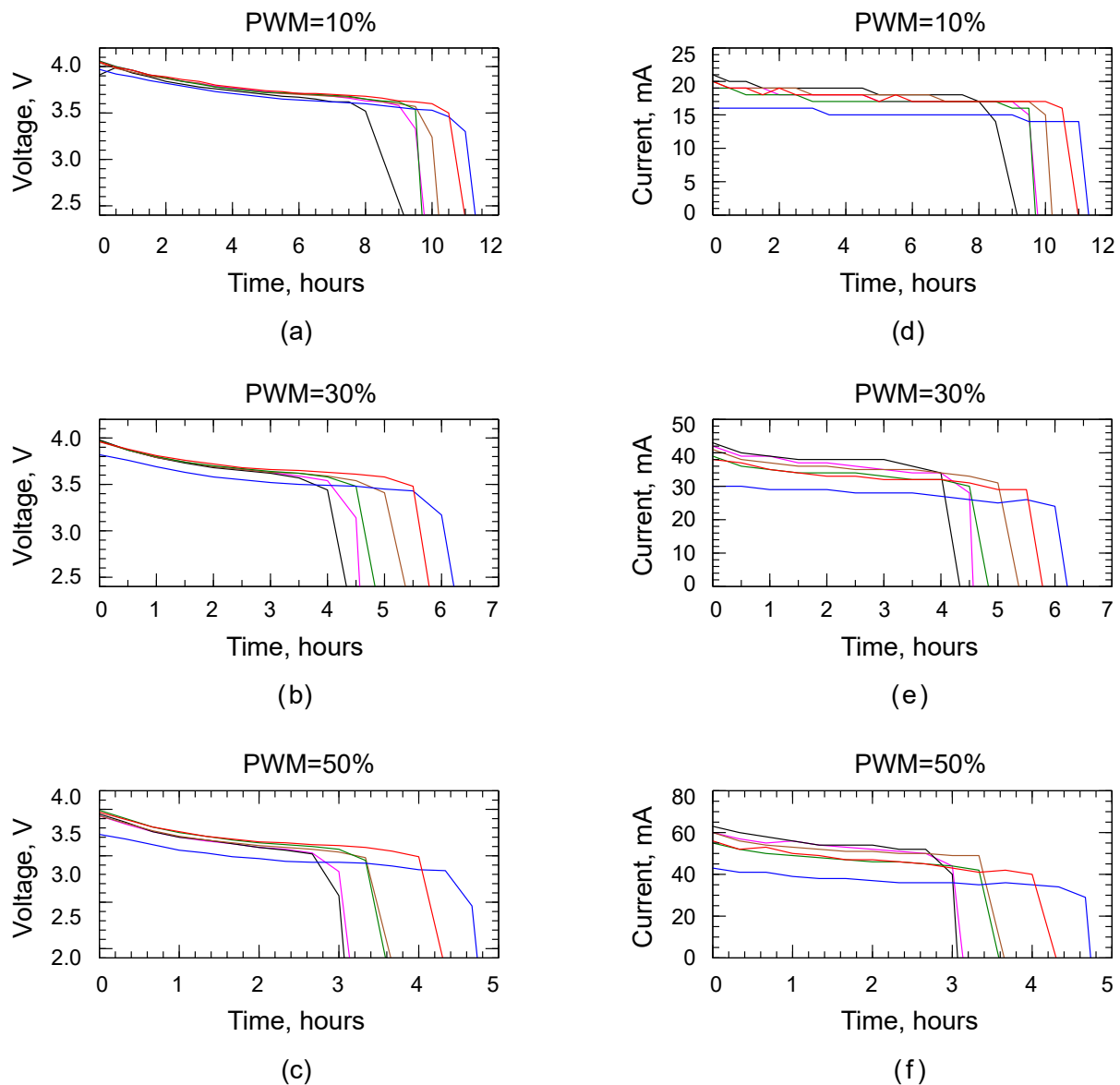


Figure S2: The measurements of the battery voltage (a-c) and current (d-f) for six Swarmodroid circuit boards working at the PWM rates 10%, 30%, and 50%, as specified in the respective panels. Different colors correspond to six different circuit boards. The matching of color to the board is the same throughout the panels.

S2 – ALGORITHM OF THE ROBOT FIRMWARE

This section offers a simplified, but complete description of the algorithm that the MCU firmware follows. For comments concerning the implementation of this algorithm on an ATTiny13 unit, see Sec. S3

To describe the MCU firmware¹, let us divide it into into the following three parts: the `main` procedure, the 8-bit Timer/Counter and the interrupt service routines (ISR) that it executes, and the pin change interrupt ISR.

S2.1 – The main procedure

The `main` procedure is executed at the moment the MCU is powered on, and follows the flowchart shown in Fig. S3. After initialization of the analog-digital converter (ADC), a self-test is performed to make sure that the battery voltage is above the critical level (approximately 3.3 V). First, the battery voltage level is measured with the motor powered off. The measured battery idle voltage is indicated by blinking the LED (D1) one time for a low charge level, two times for a medium level, and three times for a full charge, respectively. If it is below the critical level, the rest of the startup sequence is skipped.

As the next step of the startup sequence, a variable is allocated to store the previous reading of the 8-bit Timer/Counter; pin-change interrupt is enabled; the 8-bit Timer/Counter is set to free-run mode and started, enabling the PWM and IR remote control receive. After that, the PWM gate output is set to high for 50 ms, making the motor run at full power. A battery level measurement is performed at the same time to ensure the battery level at full load does not fall below the critical level. Finally, Timer/Counter overflow interrupt is enabled, and the corresponding ISR is set to perform a battery level measurement; the device waits for one second, enables global interrupts and lits up the LED to indicate the end of the startup sequence.

Now the device enters an infinite loop, which checks the battery voltage every second and does nothing else. All bot functionality is now performed by the interrupt service routines. If the battery level falls down to the critical level, the loop breaks and the bot enters the power-saving mode.

Upon entering this mode, the PWM output is forced constant low, the LED is turned off and all interrupts are globally disabled to make the bot unresponsive to any commands. After that, the LED is turned off and blinked briefly every three seconds to indicate that the bot needs to be charged.

¹ <https://github.com/swarmtronics/swarmdroid.firmware>

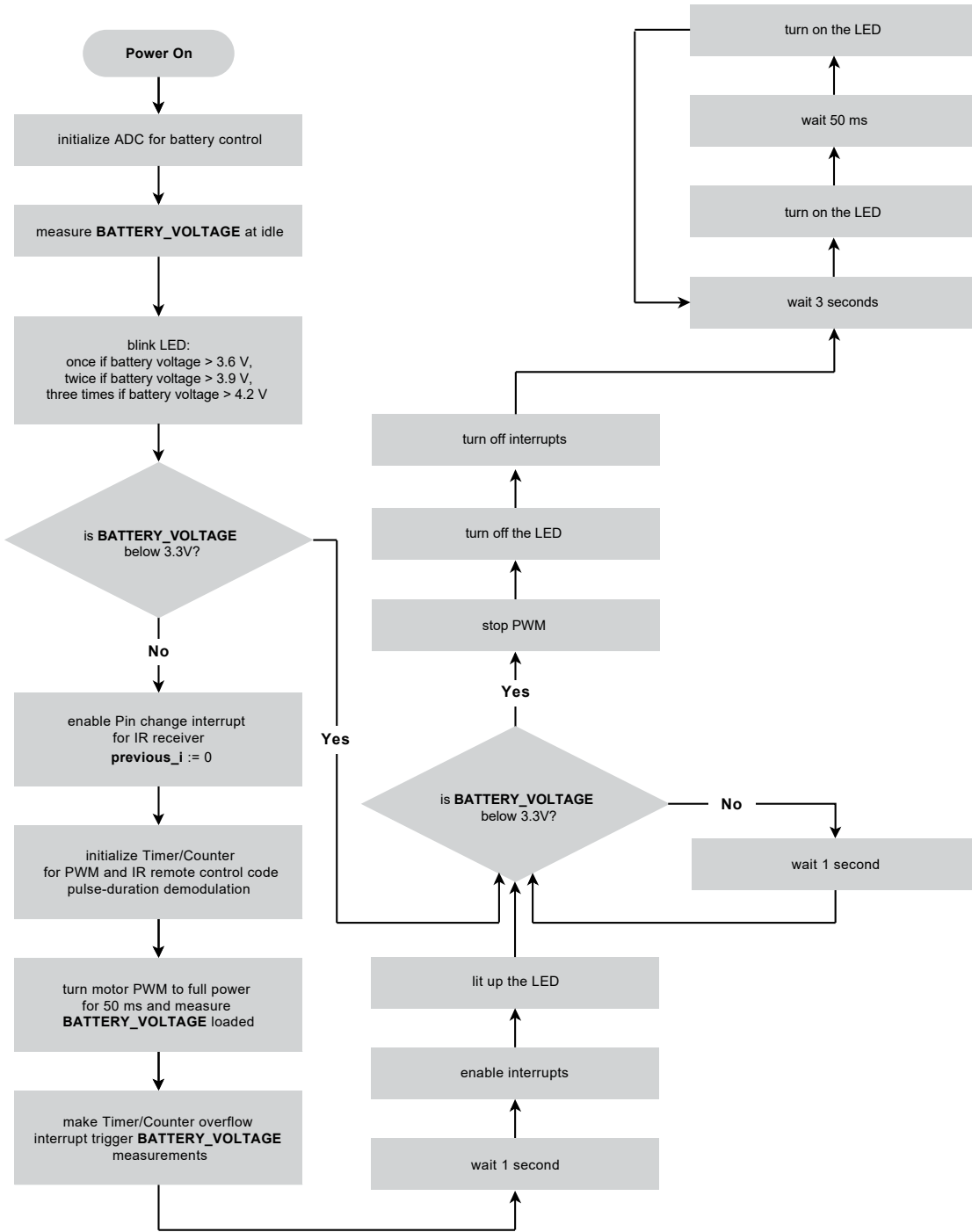


Figure S3: Flowchart of the bot firmware main procedure.

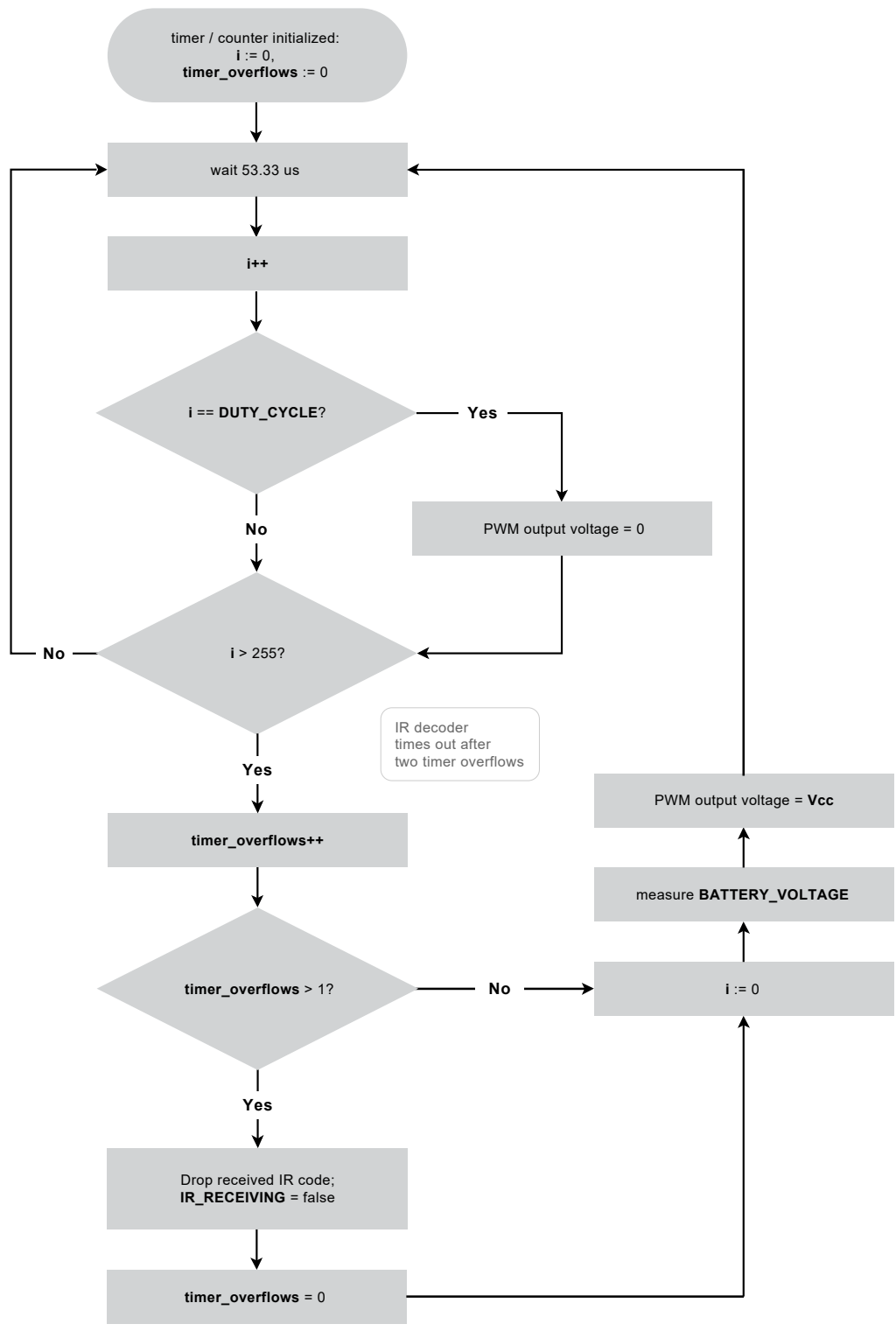


Figure S4: Flowchart of the bot firmware 8-bit Timer/Counter.

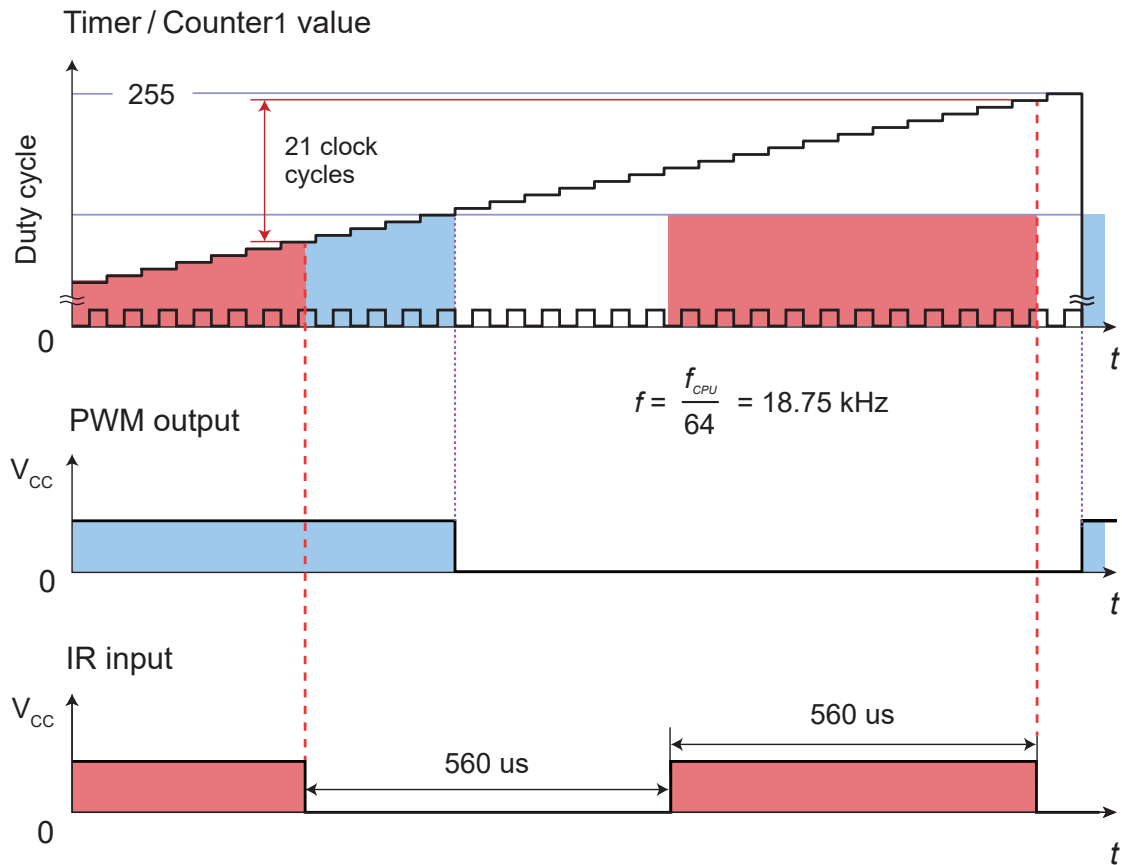


Figure S5: Timing diagram of the bot microcontroller unit.

S2.2 – 8-bit Timer/Counter

The microcontroller runs at the frequency $f_{CPU} = 1.2 \text{ MHz}$ (9.6 MHz from internal RC oscillator divided by 8 by the CKDIV8 prescaler, as defined by the FUSEs ATTiny13A is shipped with). The Timer/Counter1 runs with a frequency equal to $f_{CPU}/64$, as defined by the software-programmed prescaler setting – i.e., at $f = 18.75 \text{ kHz}$. Each 53.3 μs the 8-bit Timer/Counter value is incremented.

While the main loop is running, the Timer/Counter is used simultaneously to generate the PWM signal, measure the pulse widths to demodulate the signal from the IR receiver, and to trigger periodic battery voltage checks. Its functionality can be demonstrated by a flowchart shown in Fig. S4. The timing diagram of the Timer/Counter is shown in Fig. S5.

S2.2.0a – PWM signal generation This Timer/Counter1 value is used to drive the PWM signal for the motor. Before starting the PWM, the 8-bit duty cycle is programmed. The PWM is then made to free-run. When the Timer/Counter1 value overflows, the PWM output is set to high. When the Timer/Counter1 value becomes equal to the programmed duty cycle value, the PWM output is set to low. Therefore, the PWM frequency is $f_{CPU}/64/256 \simeq 73 \text{ Hz}$ with 256 possible duty cycle values.

S2.2.0b – Periodic battery level checks At the Timer/Counter1 overflow event, a measurement of the loaded battery voltage using the ADC is triggered right after setting the PWM output to high. The resulting value is checked in the main loop.

S2.2.0c – Pulse-period demodulation The demodulation is mostly performed in the pin change interrupt ISR, described in detail in Sec. S2.3. The Timer/Counter carries two functions for the demodulation. First, the Timer/Counter's value is used for time measurement. To measure the time interval between two incoming falling pulse edges, the difference with its previous value, stored into a variable, is calculator in the pin change interrupt ISR.

The second function is the overflow counter. There is no pulse sequence in the NEC protocol, that is longer than $256 \times 53.3 \mu\text{s}$. Therefore, to avoid locking the pulse-period demodulation state machine locking in the “receiving 32 data bits” state if the transmission is aborted before 32 bits has been received, an automatic reset is needed if too

much time has passed since the last pulse edge. The second Timer/Counter1 overflow is used as the definition of “too much time”, as the measurement by calculating the difference becomes meaningless anyway if more than one overflow has occurred.

To achieve that, an overflow counter is used. It is incremented at overflow events and reset to zero in the pin change interrupt service routine. Therefore, the overflow counter contains the number of Timer/Counter1 overflows since the last measurement. At Timer/Counter1 overflow event, the overflow counter is incremented. If, after the increment, the overflow counter reaches two, the state machine is reset from the “receiving 32 data bits” state to the “receiving not initiated” state.

S2.3 – Pin change interrupt ISR

The NEC infrared transmission protocol uses the pulse-period modulation: after the initial pulse sequence, 32 bits of data are transmitted, encoded as $(560 \mu\text{s}\downarrow + 560 \mu\text{s}\uparrow)$ pulse pair for logical 0 and $(560 \mu\text{s}\downarrow + 1680 \mu\text{s}\uparrow)$ for logical 1 (here \uparrow indicates 3.3 V level and \downarrow indicates 0 V). The decoding is performed by measuring the distances between the falling pulse edges using Timer/Counter1 and processing them using a finite state automaton (FSA).

A pin-change interrupt is enabled on the pin that is connected to the infrared receiver output, so that an interrupt event is generated at each change of the logical level. At each pin change interrupt event, the corresponding interrupt service routine is executed and performs the actions shown by the flowchart in Fig. S6 to alter the state of the FSA according to the meaning of the received pulse.

First, the sign of the edge that caused the interrupt, is checked. Rising edges are ignored, except for the 4.5 ms \uparrow leading pulse (the lengths of the positive and negative pulses are measured separately in this case). If the interrupt was caused by a falling edge, the Timer/Counter1 value is stored to the `previous_TCNT1` variable. By calculating the difference between the current Timer/Counter1 value and the `previous_TCNT1` (overflow is permitted at this point), the pulse period (the distance between the falling edges) is measured within $\pm 50 \mu\text{s}$ accuracy. In the NEC IR protocol, all meaningful pulse widths are multiples of $560 \mu\text{s}$ – up to the longest (9 ms \downarrow + 4.5 ms \uparrow) pulse pair, which is approximately $253 \times 53.3 \mu\text{s}$. Therefore, such a measurement allows to discriminate between all pulse pairs occurring in the NEC protocol.

After the length of the positive-negative pulse pair has been measured, its meaning is analyzed. If it was a transmission-initiating sequence (9 ms \downarrow + 4.5 ms \uparrow), then the FSA is put into the *receiving* state, and the shift register, which will hold the received value, is cleared.

If a pulse pair other than the transmission-initiating sequence has been received when the FSA is in the *non-receiving* state, it is ignored.

If the received pulse pair corresponds to either logical 0 ($560 \mu\text{s}\downarrow + 560 \mu\text{s}\uparrow$) or logical 1 ($560 \mu\text{s}\downarrow + 1680 \mu\text{s}\uparrow$) while the FSA is in the *receiving* state, the corresponding bit is shifted into the shift register. The shift register is then checked whether it contains all 32 bits. If not, nothing else is done. If all 32 bits have been received, the FSA is put to the *non-receiving* state, and the received bits are processed in the following way. The first (most-significant) 16 bits are compared to the hard-coded 16-bit address constant of the bot. If those are not equal, the command is understood as directed to some other device and is ignored. Next, the command, which is contained in the third byte, is checked for being valid by comparing it to the logical inverse of the fourth byte. If those are equal, the command is valid. It is then searched in the list of known commands, and, if found, the corresponding PWM duty cycle is chosen. In case the corresponding duty cycle is zero, the PWM output is driven to constant zero, and an indication of the battery voltage is performed.

If any other pulse pair is received in the *receiving* state, the entire pulse sequence is dropped and the FSA is reset into the *non-receiving* state.

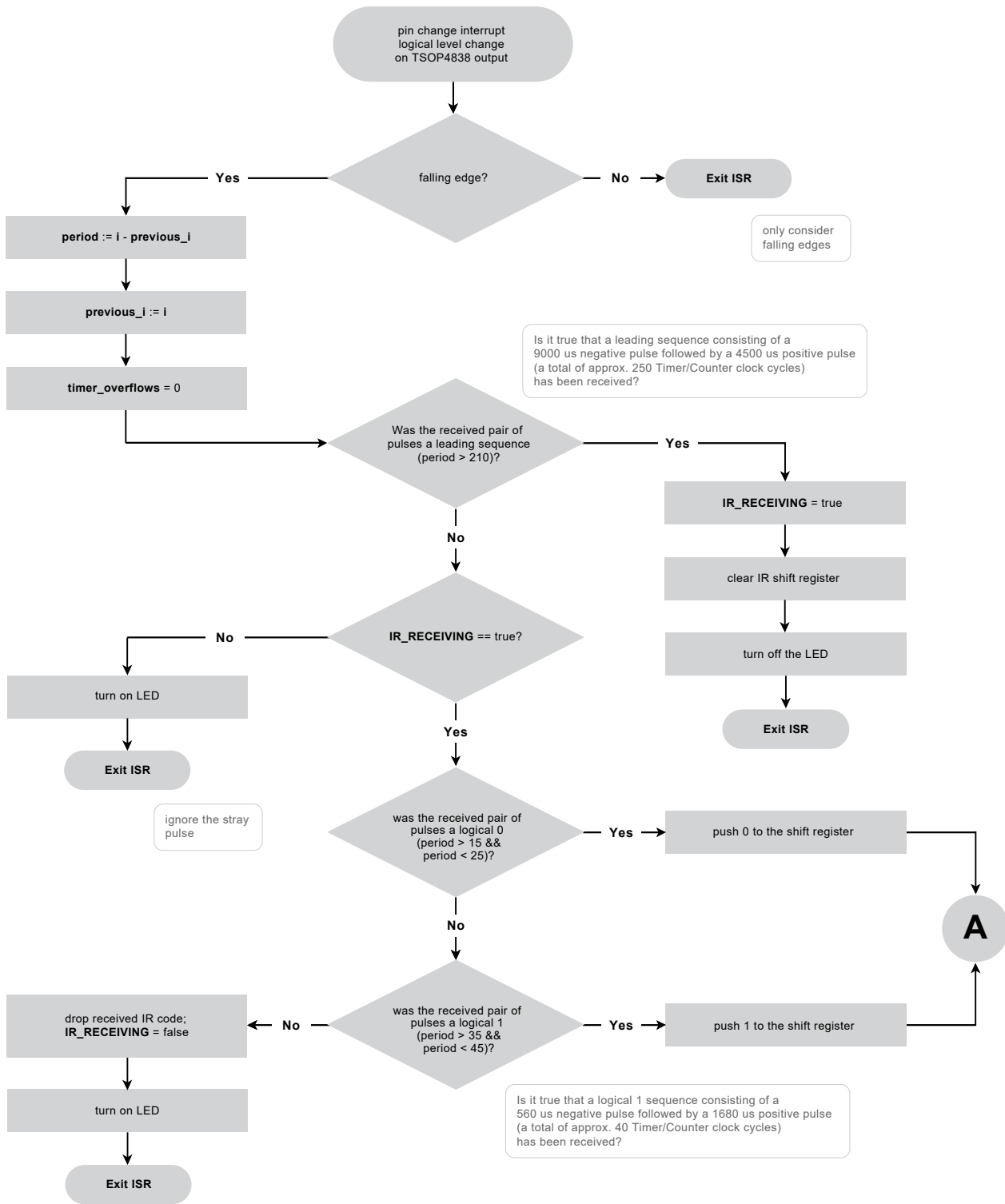


Figure S6: Flowchart of the bot firmware interrupt service routine (ISR) executed at pin change interrupt events.

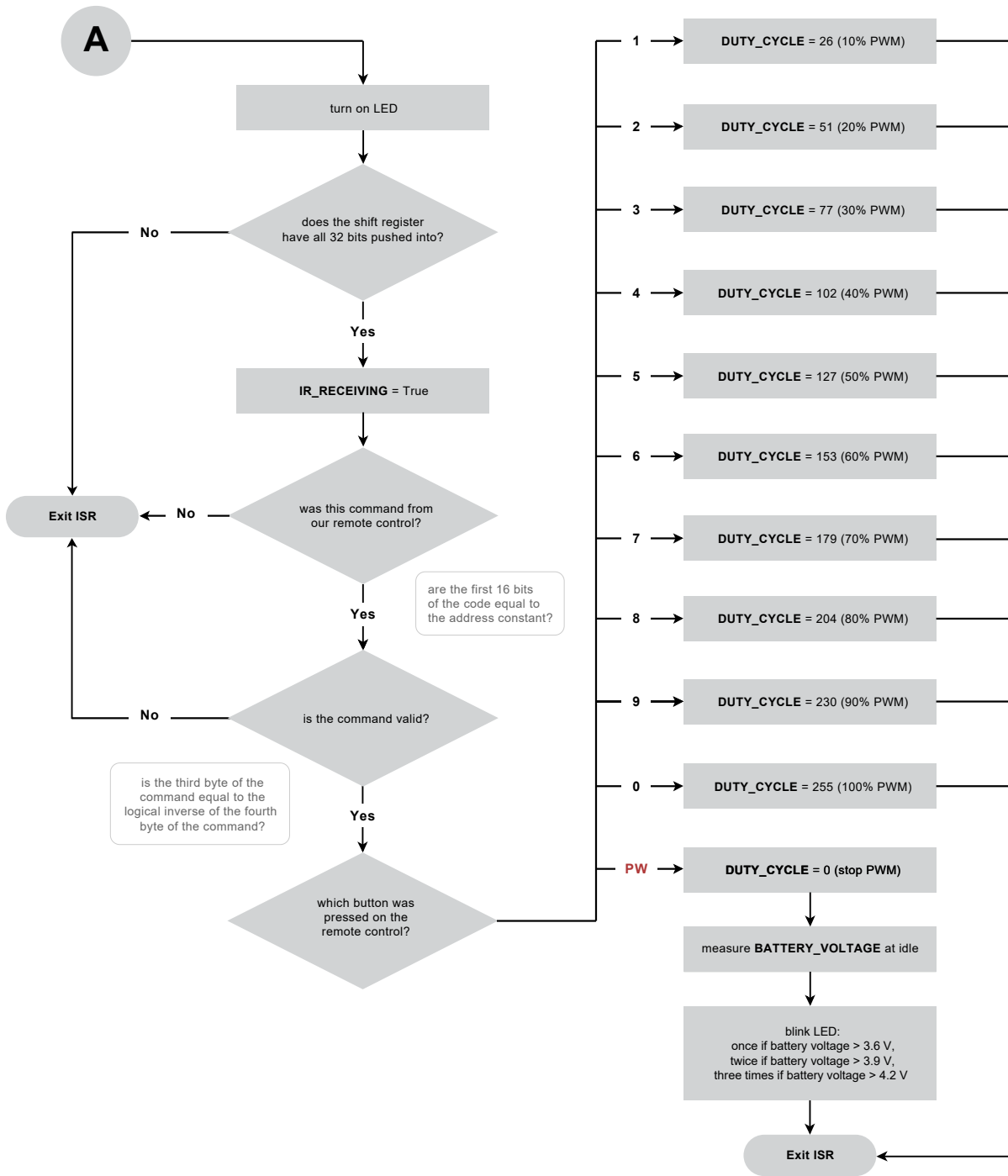


Figure S6 (continued): Flowchart of the bot firmware interrupt service routine (ISR) executed at pin change interrupt events.

S3 – FIRMWARE REFERENCE

Here, a detailed description of each code block of the firmware is provided. Firmware is originally written in the C programming language, using the `avr-libc` library and is verified to compile correctly with `avr-gcc 5.4.0` with the following options:

```
avr-gcc -mmcu=attiny13 -O2 -fshort-enums main.c
```

Note that the assembler code listed in this document has been partially changed to increase readability, and, while it performs the same actions, it does not correspond exactly to the object file produced by `avr-gcc`.

S3.1 – Global variables

As the firmware relies heavily on the interrupts, it utilizes global volatile variables allocated in the heap, along with the registers. The following global variables are defined.

S3.1.0a – State of the IR demodulator FSA

C code

```
1 typedef enum {
2     IR_STATE_IDLE,
3     IR_STATE_LEADING_9000ms,
4     IR_STATE_LEADING_4500ms,
5     IR_STATE_DATA_BITS
6 } ir_state_t;
7
8 volatile ir_state_t ir_state = IR_STATE_IDLE;
```

Assembler code

```
1 /* .section .bss */
2 .global ir_state
3 .type ir_state, @object
4 .size ir_state, 1
5 ir_state:
6 .zero 1
7
8 .equ IR_STATE_IDLE, 0
9 .equ IR_STATE_LEADING_9000ms, 1
10 .equ IR_STATE_LEADING_4500ms, 2
11 .equ IR_STATE_DATA_BITS, 3
```

The global variable `ir_state` holds the current state of the IR pulse-period demodulator state machine. The following states are possible:

0. `IR.STATE.IDLE` – the IR receiver output is held constantly at V_{CC} . The bot is waiting for a falling edge that initiates an incoming transmission. This is the default state.
1. `IR.STATE.LEADING_9000ms` – an incoming transmission falling edge has been encountered, a 9 ms logical low leading pulse now being received – the bot is now waiting for a rising edge.
2. `IR.STATE.LEADING_4500ms` – a 9 ms logical low leading pulse has been completely received, now a 4.5 ms logical high leading pulse is being received – the bot is now waiting for a falling edge.
3. `IR.STATE.DATA_BITS` – the 32 data bits are now being received. At this state, only full periods (falling edge to falling edge) are measured, so the timer is only read on falling edges. Rising edges are ignored at this state. When all 32 bits are successfully received, the FSA will be reset to `IR.STATE.IDLE`. The same will happen if an unexpected pulse sequence is encountered, with the only exception of a leading 9 ms pulse – in that case, the FSA is put back at `IR.STATE.LEADING_9000ms`.

S3.1.0b – IR shift register

C code

```

1 uint32_t ir_shift_register = 0;
2 volatile uint8_t ir_received_bits_count = 0;

```

Assembler code

```

1 /* .section .bss */
2 .global ir_shift_register
3 .type ir_shift_register, @object
4 .size ir_shift_register, 4
5 ir_shift_register:
6 .zero 4
7 .global ir_received_bits_count
8 .type ir_received_bits_count, @object
9 .size ir_received_bits_count, 1
10 ir_received_bits_count:
11 .zero 1

```

The global variable `ir_shift_register` is a 32-bit shift register that incoming IR 32-bit pulse sequences are clocked into. `ir_received_bits_count` is a counter that is used to stop receiving bits when all 32 bits are received, and which is also reset to zero to drop any bit sequences that have not been completely received due to a timeout or a malformed pulse sequence.

S3.1.0c – Timer/Counter previous value

C code

```

1 volatile uint8_t previous_TCNT0_value = 0;
2 volatile uint8_t timer_overflow_flag;

```

Assembler code

```

1 /* .section .text */
2 .comm timer_overflow_flag,1,1
3
4 /* .section .bss */
5 .global previous_TCNT0_value
6 .type previous_TCNT0_value, @object
7 .size previous_TCNT0_value, 1
8 previous_TCNT0_value:
9 .zero 1

```

The global variable `previous_TCNT0_value` holds the previous value of the 8-bit Timer/Counter. The current value is stored by the timer in the register `TCNT0`. The global flag variable `timer_overflow_flag` is a 1-bit overflow counter, which indicates a non-zero count of Timer/Counter overflows happened since the last time `TCNT0` has been stored into `previous_TCNT0_value` using the macro `start_time_interval_measurement()` or `get_time_interval_since_last_measurement()`. If this flag is set, at a subsequent Timer/Counter overflow event, handled by the Timer/Counter overflow interrupt service routine, the received IR bits will be dropped due to a timeout. The reason is that we use the difference between the current timer/counter value and its previous value to measure the pulse widths. This allows correct measurement even if a timer overflow has happened once, but not twice. We therefore use the second overflow as a trigger to hang up the IR receive.

S3.1.0d – Battery critical discharge flag

C code

```

1 volatile uint8_t battery_status_critical;

```

Assembler code

```

1 /* .section .text */
2 .comm battery_status_critical,1,1

```

The global flag variable `battery_status_critical` indicates that the battery voltage has fallen down to a critical level. This variable is updated and read in an asynchronous manner. First, at a Timer/Counter overflow event, an ADC measurement is triggered by the auto-trigger function. As soon as the measurement is finished, the ADC measurement complete interrupt service routine updates the `battery_status_critical` variable by executing the macro `ensure_battery_level_above_critical()`. Finally, this flag is read each second in the main loop, which is terminated as soon as the flag is read as set.

S3.2 – Macro definitions: hardware-related constants

S3.2.0a – Time bases First, we define the constants related to the MCU clock frequency.

C code

```
1 #define F_CPU 1200000UL
2 #define F_CPU_ACCURACY_PERCENT 20
```

Assembler code

```
1 .equ F_CPU, 1200000
2 .equ F_CPU_ACCURACY_PERCENT, 20
```

The constant `F_CPU` is defined to be equal to the MCU clock frequency in Hz, as a 4-bit unsigned integer number. In our case, the MCU runs at factory fuses: 9.6 MHz frequency with `CKDIV8` (divide the clock frequency by 8) enabled, therefore the CPU is clocked at 1.2 MHz. This constant is used as a general time base for milliseconds to clock cycles conversion to create delays and for microseconds to Timer/Counter ticks conversion for pulse-period demodulation of the IR signals.

The constant `F_CPU_ACCURACY_PERCENT` is defined to simplify the conversion from the number of Timer/Counter cycles to the actual time in microseconds using macros. We assume the 20% accuracy of the CPU frequency, as the MCU is clocked using its internal RC oscillator, which we do not calibrate.

C code

```
1 #define TCNT_PRESCALER 64
```

Assembler code

```
1 .equ TCNT_PRESCALER, 64
```

This macro carries the value of the Timer/Counter prescaler. We set the Timer/Counter to run at $f = F_{\text{CPU}}/64 = 18.75$ kHz.

S3.2.0b – Pin function constants

C code

```
1 #define BIT_PWM 1
2 #define BIT_LED 2
3 #define BIT_IR 3
4 #define BIT_ADC 4
```

Assembler code

```
1 .equ BIT_PWM, 1
2 .equ BIT_LED, 2
3 .equ BIT_IR, 3
4 .equ BIT_ADC, 4
```

These macros match the bits of `PORTB` and the corresponding electronic components (MOSFET gate, LED, output of the IR receiver and the voltage divider for battery level measurements, respectively) on the actual printed circuit board. Note that the PWM pin doubles as `OCROB` (the Timer/Counter PWM output).

S3.2.0c – Battery charge levels

C code

```
1 #define BATTERY_CRITICAL 131
2 #define BATTERY_LEVEL_SPACING 12
```

Assembler code

```
1 .equ BATTERY_CRITICAL, 131
2 .equ BATTERY_LEVEL_SPACING, 12
```

The first macro holds the `ADCH` reading (the most-significant byte of the ADC reading, while the value is left-adjusted) corresponding to the critical battery level. The second value holds the spacing between the battery levels, in `ADCH` reading units. These constants are obtained as follows. The ADC is multiplexed to the pin, which is connected to V_{CC} through a $R_1 : R_2$ resistor voltage divider. Therefore, the 10-bit ADC reading equals

$$\text{ADC} = 1024 \cdot \frac{V_{\text{CC}}}{V_{\text{ref}}} \frac{R_1}{R_1 + R_2},$$

where $R_1 = 680 \Omega$ and $R_2 = 3300 \Omega$ are the values of the resistors in the voltage divider, and $V_{\text{ref}} = 1.1 \text{ V}$ is the voltage provided by the MCU built-in bandgap reference. We configure the ADC for left-aligned 10-bit-in-uint16 storage, therefore

$$\text{ADCW} = \text{ADC} \ll 6 \text{ (16-bit value)},$$

$$\text{ADCH} = (\text{ADCW} \gg 2) \& 0\text{xFF}.$$

The ADC and ADCH readings corresponding to each of the four defined battery levels is, therefore, defined according to Table S1, and the spacing between the levels is 12.

Battery level	V _{CC}	ADC reading (decimal)	ADCH reading (decimal)
critical	3.3 V	524	131
low	3.6 V	572	143
medium	3.9 V	620	155
full	4.2 V	668	167

Table S1: Battery levels indicated by the Swarmodroid and the corresponding ADC readings.

S3.2.0d – ADC multiplexer helper macros

C code

```
1 #define ADC_ON_PB2 1
2 #define ADC_ON_PB3 3
3 #define ADC_ON_PB4 2
4 #define ADC_ON_PB5 0
```

Assembler code

```
1 .equ ADC_ON_PB2, 1
2 .equ ADC_ON_PB3, 3
3 .equ ADC_ON_PB4, 2
4 .equ ADC_ON_PB5, 0
```

Finally, we define ADC multiplexer constants, to select the pin the ADC will be listening to. Refer to the description of the ADCMUX register in the ATTiny13A documentation [1].

S3.3 – Macro definitions: inline functions

S3.3.0a – Delay loops The firmware relies on empty loops to create delays. In the C code, the utility macros defined in `util/delay.h` are used. In assembly code, we define our own macros for delay creation.

C code

```
1 #include <avr/interrupt.h>
2 #include <util/delay.h>
```

In C code, the headers `avr/interrupt.h` and `util/delay.h` containing macro definitions from the `avr-libc` are included. For `util/delay.h` to work properly, the constant `F_CPU` must be defined prior to inclusion of `util/delay.h` and set to correspond to the actual clock frequency of the device.

In assembler code, one may define the following two macros to substitute those defined in `util/delay.h`. As in the C code, the constant `F_CPU` must be defined earlier.

Assembler code

```
1 .macro delay16bit_r24_r25 delay_ms
2   .set DELAY, (F_CPU / 4000 * delay_ms - 1)
3   ldi r24, lo8(DELAY)
4   ldi r25, hi8(DELAY)
5   1: sbiw r24, 1
6   brne 1b
7   rjmp .
8   nop
9 .endm
```


Assembler code

```

1  .macro delay24bit delay_ms reg1 reg2 reg3
2      .set DELAY, (F_CPU / 5000 * delay_ms - 1)
3      ldi \reg1,lo8(DELAY)
4      ldi \reg2,hi8(DELAY)
5      ldi \reg3,hlo8(DELAY)
6      1:
7      subi \reg1,1
8      sbci \reg2,0
9      sbci \reg3,0
10     brne 1b
11     rjmp .
12     nop
13 .endm

```

S3.3.0b – LED signalling The following macros, defined for code readability, correspond to switching the LED on and off.

C code

```

1  #define led_on() { \
2      PORTB |= 1 << BIT_LED; \
3  }

```

Assembler code

```

1  .macro led_on
2      sbi PORTB, BIT_LED
3  .endm

```

C code

```

1  #define led_off() { \
2      PORTB &= ~(1 << BIT_LED); \
3  }

```

Assembler code

```

1  .macro led_off
2      cbi PORTB, BIT_LED
3  .endm

```

S3.3.0c – PWM on/off

C code

```

1  #define pwm_start() { \
2      PORTB |= (1 << BIT_PWM); \
3      DDRB |= (1 << BIT_PWM); \
4  }
5

```

Assembler code

```

1  .macro pwm_start
2      sbi PORTB, BIT_PWM
3      sbi DDRB, BIT_PWM
4  .endm

```

This macro enables the PWM by unlocking the write operations to the corresponding pin of PORTB, and puts the PWM output to logical high.

C code

```

1  #define pwm_stop() { \
2      PORTB &= ~(1 << BIT_PWM); \
3      DDRB &= ~(1 << BIT_PWM); \
4  }

```

Assembler code

```

1  .macro pwm_stop
2      cbi PORTB, BIT_PWM
3      cbi DDRB, BIT_PWM
4  .endm

```

This macro forces the PWM output to logical low and locks the corresponding pin of PORTB for write operations, thus force switching the PWM off.

S3.3.0d – IR hangup

C code

```
1 #define ir_hangup() { \
2     ir_state = IR_STATE_IDLE; \
3     led_on(); \
4 }
```

Assembler code

```
1 .macro ir_hangup
2     sts ir_state, __zero_reg__
3     led_on
4 .endm
```

This macro is used to drop the IR received bits. The FSA is reverted to the non-receiving (idle) state, and the LED is switched back on.

S3.3.0e – Time interval measurement

C code

```
1 #define start_time_interval_measurement() \
2     previous_TCNT0_value = TCNT0; \
3     timer_overflow_flag = 0
```

Assembler code

```
1 .macro start_time_interval_measurement reg
2     in \reg, TCNT0
3     sts previous_TCNT0_value, \reg
4     sts timer_overflow_flag, __zero_reg__
5 .endm
```

This macro remembers the current Timer/Counter reading (TCNT0) into the global variable `previous_TCNT0_value` that stores its previous value. The timer overflow counter is also reset to zero.

C code

```
1 #define get_time_interval_since_last_measurement() \
2     TCNT0 - previous_TCNT0_value; \
3     start_time_interval_measurement()
```

Assembler code

```
1 .macro get_time_interval_since_last_measurement out reg
2     in \out, TCNT0
3     lds \reg, previous_TCNT0_value
4     sub \out, \reg
5     start_time_interval_measurement \reg
6 .endm
```

The second macro does the same as the first one, while also returning the time interval since the previous measurement.

S3.3.0f – Setting PWM duty cycle

C code

```
1 #define pwm_set_duty_cycle(duty_cycle) { \
2     OCR0B = duty_cycle; \
3     if(duty_cycle){ \
4         pwm_start(); \
5     } else { \
6         pwm_stop(); \
7         measure_and_show_battery_idle_voltage(); \
8     } \
9 }
```

Assembler code

```
1 .macro pwm_set_duty_cycle pwmreg exitlabel
2     out OCR0B, \pwmreg
3     tst \pwmreg
4     breq if
5     pwm_start
6     rjmp \exitlabel
7     1:
8     pwm_stop
9     rcall measure_and_show_battery_idle_voltage
10    rjmp \exitlabel
11 .endm
```

This macro updates the duty cycle register `OCR0B`, while treating the zero duty cycle case in a special manner. As the smallest duty cycle supported by the Timer/Counter PWM is $1/256$, to avoid voltage spikes at zero duty cycle, the PWM output is explicitly forced low in this case. For convenient battery level checking, the battery voltage is

also indicated by LED blinking, if a zero duty cycle has been selected.

S3.3.0g – Battery level measurement

C code

```
1 #define adc_fire_once(){ \
2     ADCSRA |= (1 << ADSC); \
3     loop_until_bit_is_set(ADCSRA, ADIF); \
4 }
```

Assembler code

```
1 .macro adc_fire_once
2     sbi ADCSRA, ADSC
3     1: sbis ADCSRA, ADIF
4     rjmp 1b
5 .endm
```

Launch the ADC once and wait for it to finish in a synchronous manner. The 10-bit reading will be stored in the 16-bit register ADCW.

C code

```
1 #define ensure_battery_level_above_critical() { \
2     if (ADCH <= BATTERY_CRITICAL) { \
3         pwm_stop(); \
4         battery_status_critical = 1; \
5     } \
6 }
```

Assembler code

```
1 .macro ensure_battery_level_above_critical reg
2     in \reg, ADCH
3     cpi \reg, (BATTERY_CRITICAL+1)
4     brsh 1f
5     cbi PORTB, BIT_PWM
6     cbi DDRB, BIT_PWM
7     ldi \reg, 1
8     sts battery_status_critical, \reg
9     1:
10 .endm
```

This macro utilizes the value ADCH previously measured by the ADC (in an asynchronous manner), to make sure that the battery level has not fallen below critical. If it did, the PWM is immediately stopped, and the global flag variable `battery_status_critical`, which is watched by the main loop, is updated to break the main loop and enter the power-saving mode.

S3.4 – Macro definitions: definitions introduced for code clarity

S3.4.0a – Microseconds to Timer/Counter cycles conversion

C code

```
1 #define usec_to_cycles(time_us, error_percent) \
2     (uint8_t) (F_CPU / 1000UL * (100 + (error_percent)) * (time_us) / TCNT_PRESCALER / 1000UL / 100)
```

Assembler code

```
1 .macro set_cycles_from_usec time_us, error_percent
2     .set CYCLES_LO, (F_CPU / 1000 * (100 - \error_percent) * (\time_us) / TCNT_PRESCALER / 1000 / 100)
3     .set CYCLES_HI, (F_CPU / 1000 * (100 + \error_percent) * (\time_us) / TCNT_PRESCALER / 1000 / 100)
4     .endm
```

This macro is used convert microseconds to Timer/Counter clock cycles (approx. 53.3 μ s) at compile time, and is introduced for code readability: so that times are explicitly written in microseconds in code. As the CPU frequency, as well as the incoming pulse train frequency, might deviate significantly from the configured value, we introduce a second argument `error_percent`, which is the supposed deviation in an integer number of percents. This is used to compute intervals, given by the CPU frequency accuracy. The usage is to compare the time interval measured by the Timer/Counter to the expected time interval, for example:

C code

```

1 uint8_t time_interval =
2   get_time_interval_since_last_measurement();
3 if ((time_interval < usec_to_cycles(60, +20))
4     && (time_interval > usec_to_cycles(60, -20)))
5   puts("time interval is 60 microseconds +/- 20%");

```

Assembler code

```

1 get_time_interval_since_last_measurement r24 r25
2 set_cycles_from_usec 60, 20
3 ldi r25,lo8(-CYCLES_LO - 1)
4 add r25,r24
5 cpi r25,lo8(CYCLES_HI - CYCLES_LO - 1)
6 brsh .+2
7 rjmp time_interval_length_in_60usec_20percent_limits:
8 time_interval_length_out_of_60usec_20percent_limits:

```

S3.4.0b – Function prologues and epilogues in assembler code For concise representation of function prologues and epilogues in assembler code, i.e., the creation and removal of a stack frame, the following macros are introduced:

```

1 __SP_L__ = 0x3d
2 __SREG__ = 0x3f
3 __tmp_reg__ = 0
4 __zero_reg__ = 1
5
6 .macro push_status
7   push r1
8   push r0
9   in r0,__SREG__
10  push r0
11  clr __zero_reg__
12 .endm
13
14 .macro pop_status
15  pop r0
16  out __SREG__,r0
17  pop r0
18  pop r1
19 .endm

```

The following macro `for_registers` is used to apply an operation sequentially to a given range of registers. The macros `for_register` and `eval_expr_and_for_register` are helpers used for correct expansion of arithmetic expressions.

```

1 .altmacro
2 .macro for_registers from, to, opcode
3   for_register \from, \opcode
4   .ifgt (to - from)
5     for_registers (\from+1), \to, \opcode
6   .endif
7   .iflt (to - from)
8     for_registers (\from-1), \to, \opcode
9   .endif
10 .endm
11
12 .macro for_register expr, opcode
13   eval_expr_and_for_register %expr, \opcode
14 .endm
15
16 .macro eval_expr_and_for_register number, opcode

```

```

17  \opcode r\number\()
18  .endm

```

Namely, `for_registers, push, 17, 31` saves all user registers to the stack, while `for_registers, pop, 31, 17` retrieves them in a correct first-in-last-out order.

S3.5 – Remote control constants

A separate header file `ir_remote_control_codes` defines a list of the known IR commands and the corresponding PWM duty cycles, in the form of a static array of structures, as well as the IR address.

C code

```

1  #include "ir_remote_control_codes.h"

```

Assembler code

```

1  .include "ir_remote_control_codes.defs"

```

Let us review the contents of this file in detail. First, it defines the bot IR address.

C code

```

1  #define REMOTECONTROL_ADDRESS 0x1CE3

```

Assembler code

```

1  .equ REMOTECONTROL_ADDRESS, 0x1CE3

```

The first 16 bits of all commands received from an IR remote control are first checked against this value, and if they are not equal, the command is ignored.

The second part of the `ir_remote_control_codes` file defines a list of IR command – PWM duty cycle pairs, 8 bit each. For clarity, these pairs are stored in a structure `ir_button_t`.

C code

```

1  typedef struct {
2      uint8_t command;
3      uint8_t pwm_duty_cycle;
4  } ir_button_t;

```

Assembler code

```

1  .macro ir_button_t command, pwm_duty_cycle
2      .byte \command
3      .byte \pwm_duty_cycle
4  .endm

```

The values themselves are stored in a constant list of `ir_button_t`.

C code

```

1  const ir_button_t IR_REMOTE_CONTROL_BUTTONS[] = {
2      {
3          .command = 0x48,
4          .pwm_duty_cycle = 0
5      },
6      {
7          .command = 0x80,
8          .pwm_duty_cycle = 13
9      },
10 }

```

Assembler code

```

1  .equ LIST_SIZE, 2
2  .global IR_REMOTE_CONTROL_BUTTONS
3  .section .rodata
4  .type IR_REMOTE_CONTROL_BUTTONS, @object
5  .size IR_REMOTE_CONTROL_BUTTONS, (2 * LIST_SIZE)
6  IR_REMOTE_CONTROL_BUTTONS:
7      ir_button_t 0x48, 0
8      ir_button_t 0x80, 13

```

S3.6 – measure_and_show_battery_idle_voltage function

This function measures the battery voltage in a synchronous manner and indicates it by blinking the signal LED several times: once for low level, twice for med, and three times for the high level, according to Table S1.

C code

```

1 void measure_and_show_battery_idle_voltage() {
2     adc_fire_once();
3     int8_t battery_level = ADCH - (BATTERY_CRITICAL + BATTERY_LEVEL_SPACING);
4     while(battery_level >= 0){
5         led_on();
6         _delay_ms(400);
7         led_off();
8         _delay_ms(400);
9         battery_level -= BATTERY_LEVEL_SPACING;
10    }
11 }

```

Assembler code

```

1 .equ SIGN_BIT, 7
2
3 .global measure_and_show_battery_idle_voltage
4 .type measure_and_show_battery_idle_voltage, @function
5 measure_and_show_battery_idle_voltage:
6     adc_fire_once
7     in r24, ADCH
8     subi r24, (BATTERY_CRITICAL + BATTERY_LEVEL_SPACING)
9     sbrc r24, SIGN_BIT
10    rjmp .LSHOW_BAT_VOLT_EPILOGUE
11    .LSHOW_BAT_VOLT_LOOP:
12    led_on
13    delay24bit 400 r18 r19 r25
14    led_off
15    delay24bit 400 r18 r19 r25
16    subi r24, BATTERY_LEVEL_SPACING
17    sbrs r24, SIGN_BIT
18    rjmp .LSHOW_BAT_VOLT_LOOP
19    .LSHOW_BAT_VOLT_EPILOGUE:
20    ret
21    .size measure_and_show_battery_idle_voltage, .-measure_and_show_battery_idle_voltage

```

The algorithm is as follows. First, the supply voltage is measured synchronously by executing the `adc_fire_once` macro. The higher byte `ADCH` of the measured value is then evaluated. The value is shifted relative to the critical level, as defined by the constant `BATTERY_CRITICAL`. After that, the LED is blinked for 800 ms corresponding to each battery level, while subtracting `BATTERY_LEVEL_SPACING` until the value becomes negative – the loop is terminated in this case.

S3.7 – main function

The `main` function is executed at power-up, takes no arguments and returns no values (i.e., it has a prototype `void main(void)`) and is responsible for executing the startup sequence, running an infinite waiting loop, and, as

soon as the battery is discharged to the critical level, indication of the critical level by yet another infinite loop.

Next are the code blocks executed by the `main` function, given in the order of execution.

S3.7.0a – ADC initialization To initialize the ADC, the following bits are set in the ADC control registers. ADC multiplexer control register (ADMUX):

- bit mask `ADC_ON_PB4` (2nd bit set only) – select the pin PB4 as the source of the analog signal;
- bit `REFS0` – select the internal 1.1 V bandgap reference as the source of the reference voltage;
- bit `ADLAR` – left-adjust the 10-bit conversion result in the 16-bit register `ADCW`.

ADC control register A (ADCSRA):

- bit `ADEN` – enable the Analog-Digital converter in the Single Conversion mode;
- bit mask `0x4` (3rd bit set only) – set the frequency to 1/16 of the CPU frequency (75 kHz) to ensure there is enough time for a 10-bit conversion (the ADC must not exceed 200 kHz for that).

After setting the control registers, the ADC is fired once to finish its initialization.

C code

```
1 ADMUX = ADC_ON_PB4 | (1 << REFS0) | (1 << ADLAR);
2 ADCSRA = (1 << ADEN) | 4;
3 adc_fire_once();
```

Assembler code

```
1 .global main
2 .type main, @function
3 .section .text.startup,"ax",@progbits
4 main:
5 ldi r24, 0x62
6 out ADMUX, r24
7 ldi r24, 0x84
8 out ADCSRA, r24
9 adc_fire_once
```

S3.7.0b – Initial battery level check At the initial battery level check, first, the write operations are allowed by setting the second bit of `DDRB` to enable the LED indication. Then the global variable `battery_status_critical` is initialized to zero. The function `measure_and_show_battery_idle_voltage()` is then called to indicate the battery voltage level at idle by blinking the LED. At last, the battery level is ensured to be above critical, and in case it is not, the rest of the startup sequence is skipped.

C code

```
1 DDRB |= 1 << BIT_LED;
2 battery_status_critical = 0;
3 measure_and_show_battery_idle_voltage();
4 ensure_battery_level_above_critical();
```

Assembler code

```
1 sbi DDRB, BIT_LED
2 sts battery_status_critical, __zero_reg__
3 rcall measure_and_show_battery_idle_voltage
4 ensure_battery_level_above_critical r24
```

S3.7.0c – Second part of the startup sequence In the second part of the startup sequence, the following register bits are set.

Global interrupt mask (`GIMSK`):

- bit `PCIE` – enable Pin Change Interrupt which we use to process the IR remote control codes.

Pin change interrupt mask (`PCMSK`):

- bit 3 – Select only pin 3 for Pin Change Interrupt

To enable the PWM, the 1st bit is set in `DDRB`.

Timer/Counter is then initialized for PWM generation and IR pulse decoding. The Timer/Counter serves three purposes at the same time. First, it is used to drive the PWM on the `OC0B` (PB1) pin. Second, it is used to measure

the pulse widths for the pulse-period demodulation to decode the IR remote control signals. To measure the pulse lengths, we read the Timer/Counter value and store it in the variable `previous_TCNT0_value`. By calculating the difference between the current and the previous readings, we may evaluate the pulse period. As we carefully select the Timer/Counter frequency to 18.75 kHz (54 us per tick), pulse widths from 54 us to 14 ms can be measured. The NEC IR protocol uses pulse widths from 560 us to 9 ms. We also use the Timer overflow interrupt to hang up the IR code receive as soon as the timer overflows for the second time (14 to 28 ms after the last pulse has been transmitted). Third, Timer/Counter overflows are used to trigger periodic battery level checks.

Therefore, we choose the following settings for the Timer/Counter. The Fast PWM mode with 0xFF as TOP is selected, with generation of a Non-inverting signal on pin OC0B, which is the same pin as PB1 aka PWM pin. In this mode, 8-bit clock counts from 0 to 255 and starts again at zero. When it encounters the value OCR0B, it clears the OC0B bit, and sets it high again when the counter is restarted from zero. The frequency is chosen to be 18.75 kHz (approx. 53.3 μ s per tick), which is obtained by selecting 64 as Timer/Counter prescaler, i.e., divide system clock by 64 for the Timer/Counter frequency.

Timer/Counter control register A (TCCR0A):

- bits WGM00 and WGM01 – set Fast PWM mode with 0xFF as TOP;
- bit COM0B1 – set Clear OC0B on Compare Match.

Timer/Counter control register B (TCCR0B):

- bit mask 0x3 – set 64 as Timer/Counter prescaler.

C code

```

1  if(!battery_status_critical) {
2      GIMSK = 1 << PCIE;
3      PCMSK = 1 << BIT_IR;
4      DDRB |= 1 << BIT_PWM;
5      TCCR0A = (1 << WGM01
6              | (1 << WGM00)
7              | (1 << COM0B1));
8      TCCR0B = 3;

```

Assembler code

```

1  .LIDLE_MEAS_BATTERY_ABOVECRITICAL:
2  lds r24,battery_status_critical
3  cpse r24,__zero_reg__
4  rjmp .LSTARTUP_SEQUENCE2
5  rjmp .LMAINLOOP_ENTRY
6  .LSTARTUP_SEQUENCE2:
7  ldi r24, 0x20
8  out GIMSK, r24
9  ldi r24, 0x08
10 out PCMSK, r24
11 sbi DDRB, 1
12 ldi r24, 0x23
13 out TCCR0A, r24
14 ldi r24, 0x03
15 out TCCR0B, r24

```

S3.7.0d – Motor self-test Perform a quick self-test: briefly turn on the motor to full power and measure the loaded battery voltage. To achieve that, we explicitly set the Timer/Counter Duty cycle (OCR0B) to 255 (100% duty cycle) and execute `pwm_start`.

C code

```

1  OCR0B = 255;
2  pwm_start();
3  _delay_ms(50);
4  adc_fire_once();
5  ensure_battery_level_above_critical();
6  pwm_stop();

```

Assembler code

```

1  ldi r24, 255
2  out OCR0B, r24
3  pwm_start
4  delay16bit_r24_r25 50
5  adc_fire_once
6  ensure_battery_level_above_critical r24
7  pwm_stop

```


S3.7.0e – Third part of the startup sequence At the third part of the startup sequence, periodic battery level checks are enabled by using the Timer/Counter overflow (i.e., the moment when the PWM opens the transistor - we want the loaded voltage for critical discharge checks) as the trigger event to start the voltage measurement. To achieve this, the following settings are loaded to the registers.

ADC control register B (ADCSRB):

- bit ADTS2 – set Timer/Counter Overflow as the ADC Auto Trigger Source.

ADC control register A (ADCSRA):

- bit ADATE – set ADC Auto Trigger Enable.

Timer interrupt mask register (TIMSK0):

- bit TOIE0 – set Timer/Counter Overflow Interrupt Enable.

C code

```

1  ADCSRB = (1 << ADTS2);
2  ADCSRA |= (1 << ADATE);
3  TIMSK0 |= (1 << TOIE0);
4  ADCSRA |= (1 << ADIE);
5  _delay_ms(1000);
6  led_on();
7  sei();
8  }
```

Assembler code

```

1  ldi r24, 0x4
2  out ADCSRB, r24
3  sbi ADCSRA, ADATE
4  in r24, TIMSK0
5  ori r24, 0x2
6  out TIMSK0, r24
7  sbi ADCSRA, ADIE
8  delay24bit 1000 r25 r18 r24
9  led_on
10 sei
11 rjmp .LMAINLOOP_ENTRY
```

S3.7.0f – Main loop The main loop is normally running forever. It is only broken out of if the battery level falls below critical. The PWM and IR remote control command receives run asynchronously, as is the battery level periodic checking, which is performed at the Timer/Counter overflow events, i.e., once in approximately 14 ms.

C code

```

1  while (!battery_status_critical){
2  _delay_ms(1000);
3  }
```

Assembler code

```

1  .LMAINLOOP:
2  delay24bit 1000 r25 r18 r24
3  .LMAINLOOP_ENTRY:
4  lds r24, battery_status_critical
5  tst r24
6  breq .LMAINLOOP
```

S3.7.0g – Power-saving mode In case the flag `battery_status_critical` becomes set, the main loop is terminated and the power-saving mode is automatically entered. In this case, the PWM output is forced to logical low, all interrupts are globally disabled by the `cli` instruction, Timer/Counter and ADC are stopped by writing zeros to the registers `TCCR0B` and `ADCSRA`. After that, an infinite loop is entered that only consists in blinking the LED for 50 ms each three seconds.

C code

```

1 pwm_stop();
2 cli();
3 TCCR0B = 0;
4 ADCSRA = 0;
5 led_off();
6 while (1){
7     _delay_ms(3000);
8     led_on();
9     _delay_ms(50);
10    led_off();
11 }

```

Assembler code

```

1 pwm_stop
2 cli
3 out TCCR0B, __zero_reg__
4 out ADCSRA, __zero_reg__
5 led_off
6 .LPOWERSAVE_LOOP:
7 delay24bit 3000 r25 r18 r24
8 led_on
9 delay16bit_r24_r25 50
10 led_off
11 rjmp .LPOWERSAVE_LOOP

```

S3.8 – Timer/Counter overflow interrupt service routine

This interrupt service routine is executed at each Timer/Counter overflow. The following actions are performed. First, an ADC single conversion is implicitly triggered on hardware level, as specified by the ADC Auto-trigger setting. Next, the `timer_overflow_flag` is set if it has not previously been. In case the flag had previously been set and not cleared by a time interval measurement, it means that the Timer/Counter has overflowed twice since the last measurement, making the next measurement meaningless. This situation is treated as an IR command timeout, and the received IR data is dropped.

C code

```

1 ISR(TIMO_OVF_vect){
2     if(timer_overflow_flag){
3         ir_hangup();
4     } else {
5         timer_overflow_flag = 1;
6     }
7 }

```

Assembler code

```

1 __vector_3:
2 push_status
3 for_registers 24 24 push
4 lds r24, timer_overflow_flag
5 cpse r24, __zero_reg__
6 rjmp .LNOT_FIRST_OVERFLOW
7 ldi r24, 1
8 sts timer_overflow_flag, r24
9 rjmp .LVECTOR3_EPILOGUE
10 .LNOT_FIRST_OVERFLOW:
11 ir_hangup
12 .LVECTOR3_EPILOGUE:
13 for_registers 24 24 pop
14 pop_status
15 reti
16 .size __vector_3, .-__vector_3

```

S3.9 – ADC conversion complete interrupt service routine

This interrupt service routine is executed each time an ADC conversion is completed. The only action it performs is to compare the measured supply voltage with the critical level and set the `battery_status_critical` flag if the measured level is lower or equal.

C code

```

1 ISR(ADC_vect){
2     ensure_battery_level_above_critical();
3 }

```

Assembler code

```

1 __vector_9:
2 push_status
3 for_registers 24 24 push
4 ensure_battery_level_above_critical r24
5 for_registers 24 24 pop
6 pop_status
7 reti
8 .size __vector_9, .-__vector_9

```

S3.10 – Pin change interrupt service routine

The logical pin change interrupt service routine is used to decode the IR remote control codes, as defined by the NEC protocol. First, the pulse-period modulated code is demodulated by measuring the pulse lengths using the Timer/Counter and analyzing them using a finite state automaton (FSA). After all 32 bits have been received, they are checked for validity and correct address, and, if these tests are passed, the PWM duty cycle corresponding to the command is set.

S3.10.0a – State machine As soon as the logical level on the IR receiver output changes, the state machine, which is implemented using a `switch` statement, is fired to analyze the current state, which is stored in the variable `ir_state`. In a correct code, a 9000 ms negative pulse must be followed by a 4500 ms positive pulse, which is in turn followed by 32 pulse pairs carrying the data bits, which can be either a (560 μ s \downarrow + 1680 μ s \uparrow) for logical 1, or (560 μ s \downarrow + 560 μ s \uparrow) for logical 0. An IR remote control also sends repeat codes if the key is held pressed, but this firmware effectively ignores them due to a timeout occurring in the absence of the data bits. If at any of the described states a wrong pulse length or polarity is found, the state machine is reset to the idle state, and the bit data is discarded.

Note: in assembler code, the edge type (one for rising and zero for falling) is stored in the register `r24`.

C code

```

1 ISR(PCINT0_vect){
2     uint8_t is_rising_edge = ((PINB >> BIT_IR) & 1);
3     switch(ir_state){
4     case IR_STATE_IDLE:
5         ...
6     case IR_STATE_LEADING_9000ms:
7         ...
8     case IR_STATE_LEADING_4500ms:
9         ...
10    case IR_STATE_DATA_BITS:
11        ...
12    }
13 }

```

Assembler code

```

1 __vector_2:
2 push_status
3 for_registers 17 31 push
4 in r24, PINB
5 bst r24, BIT_IR
6 clr r24
7 bld r24, 0
8 lds r25, ir_state
9 cpi r25, IR_STATE_LEADING_9000ms
10 brne .+2
11 rjmp .LVECTOR2_CASE_IR_STATE_LEADING_9000ms
12 brsh .+2
13 rjmp .LVECTOR2_CASE_IR_STATE_IDLE
14 cpi r25, IR_STATE_LEADING_4500ms
15 breq .LVECTOR2_CASE_IR_STATE_LEADING_4500ms
16 cpi r25, IR_STATE_DATA_BITS
17 breq .LVECTOR2_CASE_IR_STATE_DATA_BITS
18 .LVECTOR2_EPILOGUE:
19 for_registers 31 17 pop
20 pop_status
21 reti
22 .size __vector_2, .-__vector_2

```

S3.10.0b – Changes from the idle state As the IR receiver is pulled high, a transmission may only be started by a falling edge. If a transmission is started, reset the timer and the FSA is switched into the next state `IR_STATE_LEADING_9000ms`.

C code

```

1 case IR_STATE_IDLE:
2     if(!is_rising_edge){
3         start_time_interval_measurement();
4         ir_state = IR_STATE_LEADING_9000ms;
5     }
6     return;

```

Assembler code

```

1 .LVECTOR2_CASE_IR_STATE_IDLE:
2 cpse r24, __zero_reg__
3 rjmp .LVECTOR2_EPILOGUE
4 start_time_interval_measurement r24
5 ldi r24, IR_STATE_LEADING_9000ms
6 sts ir_state, r24
7 rjmp .LVECTOR2_EPILOGUE

```

S3.10.0c – Changes from the state `IR_STATE_LEADING_9000ms` This state corresponds to waiting for the end of a 9000 ms leading negative pulse, therefore a change to any of the next states may only be triggered by a rising edge. If a rising edge is encountered, the time interval between the previous falling edge and the current rising edge is measured. If its length indeed falls into the $9000\ \mu\text{s} \pm 20\%$ interval (approx. 170 Timer/Counter cycles), the FSA is switched to the next state `IR_STATE_LEADING_4500ms`. If a pulse of any other length has been observed, the state machine is reset to the `IR_STATE_IDLE` state.

C code

```

1 case IR_STATE_LEADING_9000ms:
2     if(is_rising_edge){
3         uint8_t time_interval =
4         get_time_interval_since_last_measurement();
5         if(time_interval > usec_to_cycles(9000,
6             -F_CPU_ACCURACY_PERCENT)
7             && time_interval < usec_to_cycles(9000,
8                 +F_CPU_ACCURACY_PERCENT)){
9             ir_state = IR_STATE_LEADING_4500ms;
10        } else {
11            ir_state = IR_STATE_IDLE;
12        }
13    }
14    return;

```

Assembler code

```

1 .LVECTOR2_CASE_IR_STATE_LEADING_9000ms:
2 tst r24
3 breq .LVECTOR2_EPILOGUE
4 get_time_interval_since_last_measurement r24 r25
5 set_cycles_from_usec 9000, F_CPU_ACCURACY_PERCENT
6 subi r24, (CYCLES_LO + 1)
7 cpi r24, (CYCLES_HI - CYCLES_LO - 1)
8 brsh .LVECTOR2_RESET_TO_IDLE
9 ldi r24, IR_STATE_LEADING_4500ms
10 sts ir_state, r24
11 rjmp .LVECTOR2_EPILOGUE
12
13 .LVECTOR2_RESET_TO_IDLE:
14 sts ir_state, __zero_reg__
15 rjmp .LVECTOR2_EPILOGUE

```

S3.10.0d – Changes from the state `IR_STATE_LEADING_4500ms` This state corresponds to waiting for the end of a 4500 ms leading positive pulse, therefore a change to any of the next states may only be triggered by a falling edge. If a falling edge is encountered, the time interval between the previous rising edge and the current falling edge is measured. If its length indeed falls into the $4500\ \mu\text{s} \pm 20\%$ interval (approx. 85 Timer/Counter cycles), the `ir_shift_register` is emptied and the FSA is switched to the next state `IR_STATE_DATA_BITS`.

If a pulse of any other length has been observed, the state machine is reset to the `IR_STATE_IDLE` state.

C code

```

1  case IR_STATE_LEADING_4500ms:
2      if(!is_rising_edge){
3          uint8_t time_interval =
4          get_time_interval_since_last_measurement();
5          if(time_interval > usec_to_cycles(4500,
6              -F_CPU_ACCURACY_PERCENT)
7              && time_interval < usec_to_cycles(4500,
8                  +F_CPU_ACCURACY_PERCENT)){
9              ir_state = IR_STATE_DATA_BITS;
10             ir_received_bits_count = 0;
11             ir_shift_register = 0;
12             led_off();
13         } else {
14             ir_state = IR_STATE_IDLE;
15         }
16     }
17     return;

```

Assembler code

```

1  .LVECTOR2_CASE_IR_STATE_LEADING_4500ms:
2  cpse r24, __zero_reg__
3  rjmp .LVECTOR2_EPILOGUE
4  get_time_interval_since_last_measurement r24 r25
5  set_cycles_from_usec 4500, F_CPU_ACCURACY_PERCENT
6  subi r24, (CYCLES_LO + 1)
7  cpi r24, (CYCLES_HI - CYCLES_LO - 1)
8  brlo .+2
9  rjmp .LVECTOR2_RESET_TO_IDLE
10 ldi r24, IR_STATE_DATA_BITS
11 sts ir_state, r24
12 sts ir_received_bits_count, __zero_reg__
13 sts ir_shift_register, __zero_reg__
14 sts ir_shift_register+1, __zero_reg__
15 sts ir_shift_register+2, __zero_reg__
16 sts ir_shift_register+3, __zero_reg__
17 led_off
18 rjmp .LVECTOR2_EPILOGUE

```

S3.10.0e – Changes from the state *IR_STATE_DATA_BITS* This state corresponds to high logical level and waiting for a data pulse pair, which can be either a (560 $\mu\text{s}\downarrow$ + 1680 $\mu\text{s}\uparrow$) for logical 1, or (560 $\mu\text{s}\downarrow$ + 560 $\mu\text{s}\uparrow$), therefore a change to any of the next states may only be triggered by a falling edge. In this state, rising edges are skipped, and distances between falling edges are measured, thus yielding the total length of a pulse pair. If a falling edge is ignored, the time interval between the previous and the current falling edges is measured.

C code

```

1  case IR_STATE_DATA_BITS:
2      if(is_rising_edge){
3          return;
4      }
5      uint8_t time_interval =
6      get_time_interval_since_last_measurement();
7      uint8_t new_bit;
8      if(time_interval > usec_to_cycles(560 + 560,
9          -F_CPU_ACCURACY_PERCENT)
10         && time_interval < usec_to_cycles(560 + 560,
11             +F_CPU_ACCURACY_PERCENT)){
12         new_bit = 0;
13     } else {
14         if(time_interval > usec_to_cycles(560 + 1680,
15             -F_CPU_ACCURACY_PERCENT)
16             && time_interval < usec_to_cycles(560 + 1680,
17                 +F_CPU_ACCURACY_PERCENT)){
18             new_bit = 1;
19         } else {
20             ir_hangup();
21             return;
22         }
23     }

```

Assembler code

```

1  .LVECTOR2_CASE_IR_STATE_DATA_BITS:
2  cpse r24, __zero_reg__
3  rjmp .LVECTOR2_EPILOGUE
4  get_time_interval_since_last_measurement r24 r25
5  set_cycles_from_usec (560+560), F_CPU_ACCURACY_PERCENT
6  ldi r25, (-CYCLES_LO - 1)
7  add r25, r24
8  cpi r25, (CYCLES_HI - CYCLES_LO - 1)
9  brsh .+2
10 rjmp .LVECTOR2_NEWBIT_ZERO
11 set_cycles_from_usec (1680+560), F_CPU_ACCURACY_PERCENT
12 subi r24, (CYCLES_LO + 1)
13 cpi r24, (CYCLES_HI - CYCLES_LO - 1)
14 brlo .+2
15 rjmp .LVECTOR2_IR_HANGUP
16 .LVECTOR2_NEWBIT_ONE:
17 ldi r20, 1
18 rjmp .LVECTOR2_STORE_NEW_BIT
19 .LVECTOR2_IR_HANGUP:
20 ir_hangup
21 rjmp .LVECTOR2_EPILOGUE
22 .LVECTOR2_NEWBIT_ZERO:
23 ldi r20, 0
24 .LVECTOR2_STORE_NEW_BIT:

```

If the obtained pulse length falls in the $(560 \mu\text{s} \downarrow + 560 \mu\text{s} \uparrow) \pm 20\%$ interval, it is treated as a logical 0. If it falls in the $(560 \mu\text{s} \downarrow + 1680 \mu\text{s} \uparrow) \pm 20\%$ interval, this pulse pair is treated as a logical 1. In either of the mentioned cases, the state machine remains in the IR.STATE_DATA.BITS waiting for the next data bit. If a pulse of any other length has been observed, the state machine is reset to the IR.STATE_IDLE state and all the received bits are dropped.

S3.10.0f – Shifting the bits into ir_shift_register The newly received data bit is shifted into `ir_shift_register`.

C code

```

1  ir_shift_register = (ir_shift_register << 1)
2      | new_bit;
3  ir_received_bits_count++;

```

Assembler code

```

1  .LVECTOR2_STORE_NEW_BIT:
2  lds r24,ir_shift_register
3  lds r25,ir_shift_register+1
4  lds r26,ir_shift_register+2
5  lds r27,ir_shift_register+3
6  lsl r24
7  rol r25
8  rol r26
9  rol r27
10 or r24, r20
11 sts ir_shift_register,r24
12 sts ir_shift_register+1,r25
13 sts ir_shift_register+2,r26
14 sts ir_shift_register+3,r27
15 lds r24,ir_received_bits_count
16 inc r24
17 sts ir_received_bits_count, r24
18 .LVECTOR2_CHECK_32BITS_RECEIVED:

```

S3.10.0g – Checking if all 32 bits have been received

C code

```

1  if(ir_received_bits_count == 32){
2      ir_hangup();
3      if ((ir_shift_register >> 16)
4          != REMOTECONTROL_ADDRESS){
5          return;
6      }
7      uint8_t command =
8          (uint8_t) (ir_shift_register >> 8);
9      uint8_t not_not_command =
10         (uint8_t) ~((uint8_t) ir_shift_register);
11     if (command != not_not_command) {
12         return;
13     }

```

Assembler code

```

1  .LVECTOR2_CHECK_32BITS_RECEIVED:
2  lds r24, ir_received_bits_count
3  cpi r24, 32
4  breq .+2
5  rjmp .LVECTOR2_EPILOGUE
6  ir_hangup
7  lds r24,ir_shift_register
8  lds r25,ir_shift_register+1
9  lds r26,ir_shift_register+2
10 lds r27,ir_shift_register+3
11 movw r20,r26
12 clr r22
13 clr r23
14 cpi r20, lo8(REMOTECONTROL_ADDRESS)
15 sbci r21, hi8(REMOTECONTROL_ADDRESS)
16 cpc r22, __zero_reg__
17 cpc r23, __zero_reg__
18 breq .+2
19 rjmp .LVECTOR2_EPILOGUE
20 mov r17,r25
21 com r24
22 cpse r25,r24
23 rjmp .LVECTOR2_EPILOGUE
24 .LVECTOR2_FIND_BUTTON:

```

After shifting a new data bit into `ir_shift_register`, a test is performed if all 32 data bits have been received. In case they have, the state machine is reset to the `IR_STATE_IDLE` state and the bit sequence is parsed.

It consists of 16 address bits (which may, in turn, consist of a 8 bit address followed by its logical inversion, but this is not always the case) followed by a 8-bit command, which is in turn followed by its logical inverse. We decode this here. We first verify that the address is correct (the command is from our remote control, i.e., directed to our bot, not to an air conditioner nor a projector), and then verify that `command == command_logical_inverse`, i.e., the command is a valid one.

S3.10.0h – Finding known commands In case all test have been passed, the command is searched in the list of known commands, and, if found, the corresponding duty cycle is set.

C code

```

1  uint8_t i;
2  for (i = 0;
3      i < sizeof(IR_REMOTE_CONTROL_BUTTONS)
4          / sizeof(ir_button_t);
5      i++){
6      ir_button_t maybe_this_button =
7          IR_REMOTE_CONTROL_BUTTONS[i];
8      if(command == maybe_this_button.command){
9          pwm_set_duty_cycle(
10             maybe_this_button.pwm_duty_cycle
11         );
12     }
13 }
14 }
15 }
```

Assembler code

```

1  .LVECTOR2_FIND_BUTTON:
2  ldi r28,lo8(IR_REMOTE_CONTROL_BUTTONS)
3  ldi r29,hi8(IR_REMOTE_CONTROL_BUTTONS)
4  rjmp .LVECTOR2_LOOP_OVER_BUTTONS_ENTRY
5  .LVECTOR2_LOOP_OVER_BUTTONS:
6  adiw r28,2
7  ldi r24,hi8(IR_REMOTE_CONTROL_BUTTONS + 2*LIST_SIZE)
8  cpi r28,lo8(IR_REMOTE_CONTROL_BUTTONS + 2*LIST_SIZE)
9  cpc r29,r24
10 brne .+2
11 rjmp .LVECTOR2_EPILOGUE
12
13 .LVECTOR2_LOOP_OVER_BUTTONS_ENTRY:
14 ld r24,Y
15 cpse r17,r24
16 rjmp .LVECTOR2_LOOP_OVER_BUTTONS
17 ldd r24,Y+1
18 pwm_set_duty_cycle r24 .LVECTOR2_LOOP_OVER_BUTTONS
```

[1] ATTiny13/ATTiny13V: 8-bit AVR microcontroller with 1K bytes in-system programmable flash. Datasheet, Rev. 2535J-AVR-08/10, Atmel Corporation, <https://ww1.microchip.com/downloads/en/devicedoc/doc2535.pdf>. Accessed 22 May 2023.